APPLIED RESEARCH

WILEY

Impact of turbulence modeling on the simulation of blood flow in aortic coarctation

Sarah Katz[1] | Alfonso Caiazzo[1] | Baptiste Moreau[1] | Ulrich Wilbrandt[1] |
Jan Brüning[2] | Leonid Goubergrits[2,3] | Volker John[1,4]

[1]Numerical Mathematics and Scientific Computing Research Group, Weierstrass Institute for Applied Analysis and Stochastics (WIAS), Berlin, Germany

[2]Deutsches Herzzentrum der Charité, Institute of Computer-assisted Cardiovascular Medicine, Charité – Universitätsmedizin Berlin, corporate member of Freie Universität Berlin and Humboldt Universität zu Berlin, Berlin, Germany

[3]Einstein Center Digital Future, Berlin, Germany

[4]Department of Mathematics and Computer Science, Freie Universität Berlin, Berlin, Germany

Correspondence
Sarah Katz, Weierstrass Institute for Applied Analysis and Stochastics (WIAS), Mohrenstr. 39, 10117 Berlin, Germany.
Email: sarah.katz@wias-berlin.de

Funding information
Deutsche Forschungsgemeinschaft, Grant/Award Numbers: GRK2433, 384950143

Abstract

Numerical simulations of pulsatile blood flow in an aortic coarctation require the use of turbulence modeling. This paper considers three models from the class of large eddy simulation (LES) models (Smagorinsky, Vreman, σ-model) and one model from the class of variational multiscale models (residual-based) within a finite element framework. The influence of these models on the estimation of clinically relevant biomarkers used to assess the degree of severity of the pathological condition (pressure difference, secondary flow degree, normalized flow displacement, wall shear stress) is investigated in detail. The simulations show that most methods are consistent in terms of severity indicators such as pressure difference and stenotic velocity. Moreover, using second-order velocity finite elements, different turbulence models might lead to considerably different results concerning other clinically relevant quantities such as wall shear stresses. These differences may be attributed to differences in numerical dissipation introduced by the turbulence models.

KEYWORDS

cardiovascular biomarkers, computational hemodynamics, finite element method, patient-specific modeling, turbulence modeling

1 | INTRODUCTION

Coarctation of the aorta (CoA) is a congenital heart defect consisting in a local narrowing in a portion of the aorta, resulting in hypertension of the upper body and with potentially severe complications. The most relevant diagnostic parameter for this pathology is the trans-stenotic pressure gradient/difference, which can only be measured directly via invasive catheterization. Non-invasive imaging-based techniques for assessing the severity of CoA rely on measuring patient anatomy, blood velocities and flow rates in the area by cardiac MRI or (Doppler) ultrasound echocardiography. Estimating pressure gradients from velocity information using a simplified Bernoulli equation has remained common practice well into the present century, despite its well-documented limitations.[1,2] Clinical guidelines[3,4] provide diagnostic criteria in terms of these biomarkers.

The severity of the disease does not only depend on the anatomical condition and the pressure gradient/difference, but can be assessed via different biomarkers that are related to abnormal flow conditions, such as increased flow asymmetries and abnormal oscillatory behaviors of the wall shear stresses (WSS). However, due to the relatively low spatial resolution of MRI, these biomarkers can only be quantified directly from medical imaging with reduced accuracy. Furthermore, these methods are time-consuming and costly. Numerical blood flow simulations can therefore play an important role in supporting available medical data, such as anatomical images and flow fields, for the estimation of these quantities of interest.[5,6]

The pulsatile blood flow in the ascending aorta reaches moderate to high Reynolds number (larger than 2000[7]) and the flow disturbances caused by aortic narrowing can yield to a transition to turbulence. Understanding the behavior of a turbulent flow is therefore relevant from the clinical point of view, since turbulence might have implications for the pathophysiology of vascular diseases and for the design of cardiovascular devices such as stents or artificial valves.[8,9]

The dynamics of turbulent flows spans a wide range of spatial scales, from Kolmogorov lengths of the order of 10–70 μm up to the diameter of the blood vessel. Direct numerical simulations (DNS) of the whole scale spectrum are beyond computationally affordable resolution of numerical discretizations. However, the smallest scales cannot be neglected, since otherwise a laminar flow would be simulated with the corresponding high inaccuracy of the computational results. The purpose of turbulence modeling consists in modeling the impact of the unresolved scales onto the resolved ones so that important properties of turbulent flows, like boundary layers, are present in the simulated flow fields.

A popular approach for modeling the effect of turbulence are so-called Reynolds Averaged Navier–Stokes (RANS) methods. These approaches focus only on the largest scales of motion and model all turbulent scales via additional terms in the momentum equations called Reynolds stress terms. Although their ability to predict transitional and relaminarizing types of flows has been criticized,[10] RANS methods are still popular in the context of cardiovascular simulations. Recent studies focused, for example, on evaluation of aortic WSS in a phantom model of aortic coarctation,[11] as well as on the anisotropy of turbulent blood flow in patient-specific settings.[12]

As an alternative to RANS, Large Eddy Simulation (LES) methods attempt to model the large turbulent scales, applying a convolutional low-pass filter to the Navier–Stokes equations and surrogating the effect of the small scales into explicit models for the stress tensor. Widely used models in this class are the original Smagorinsky model,[13] as well as the Vreman[14] and Nicoud[15] σ-viscosity models. In recent relevant works, a LES σ-model was used to investigate the impact of turbulence in the context of abdominal aortic aneurysms,[16] while a LES Leroy decay model was used to study the sensitivity of simulated WSS in the aorta.[17]

A conceptually different turbulence model considered in this paper is the residual-based variational multiscale approach[18] (RB-VMS). This method is based on a two-scale decomposition of the analytic function spaces for velocity and pressure, where the fine space represents the scales, which cannot be represented by the considered finite element discretization. The influence of these scales is then surrogated in the coarse dynamics using additional terms in the variational formulation. RB-VMS methods have shown promising results in recent studies of turbulent channel flows.[19] To the best of our knowledge, variational multiscale models have not yet been investigated in the context of blood flow simulation, nor are detailed studies comparing different choices available in the literature.

The question studied in this paper can be formulated as follows: using a reasonably fine computational mesh which is still affordable from the point of view of computing times, how much do results differ for several clinically relevant quantities of interest if different turbulence models are used in the discretization? This question addresses the common practical situation where a mesh of the domain is given, which is chosen fine in order to obtain accurate results, but any (uniform) refinement of the mesh is prohibitive due to the increasing computational costs.

The purpose of this work is to investigate in detail the impact of turbulence modeling on the simulation of blood flow in an aortic coarctation. In particular, LES models and RB-VMS models are considered. Exemplarily for the RB-VMS model, the impact of the order of the finite element velocity space is investigated. For the comparison, we focus on selected quantities of interest, which are commonly used to characterize abnormal or pathological flow conditions such as the variation of pressure along the aorta, the secondary flow degree, and the normalized flow displacement.[20] Furthermore, the sensitivity of the wall shear stress (WSS) and of the related oscillatory shear index (OSI) are analyzed, as these biomarkers have been linked with the deposition of atheromatous plaque in blood vessels.[21]

The numerical simulations are based on an aortic geometry obtained from medical imaging, with patient-specific boundary conditions defined using available data. In particular, measurements are limited to a space-dependent cardiac outflow profile, which is prescribed as Dirichlet inlet boundary condition, and peak outflow rates on the brachiocephalic artery, the left carotid, the left subclavian, and the descending aorta, which are used to tune lumped

parameter models. To this purpose, purely resistive outflow boundary conditions are used, and a sequential approach for the estimation of boundary condition parameters based on the available flow rates is proposed.

The remainder of the article is structured as follows. Section 2 describes the available data that were used to build the computational model and the simulation setup. Section 3 introduces the blood flow model, the numerical methods, the proposed approach for estimating boundary parameters, and the considered turbulence models. The results are presented in Section 4, while Section 5 summarizes the conclusions.

2 | MATERIALS

Available data were acquired on a 1.5T clinical MR system (Achieva; Philips Healthcare, Best, Netherlands) with a five-element cardiac phased-array coil.[6] Within the cardiac MRI protocol velocity-encoded MRI (4D VEC MRI) was acquired in planes perpendicular to the ascending aorta distally to the valve and in the descending aorta at the level of the diaphragm to assess inflow conditions in three flow encoding orientations and outflow towards the abdominal aorta.

The considered domain (Figure 1, left) for the numerical simulation consists of a portion of the aorta from the sino-tubular junction to the descending aorta at the level of the left ventricular apex (about 20 cm length).

The computational mesh was obtained by segmenting the anatomy of the aorta based on the diastolic 3D SSFP cine images using ZIBAmira (v. 2015.28, Zuse Institute Berlin, Germany), as in a previous work.[7] From the obtained surface triangular mesh, Figure 1, center and right, a tetrahedral volume mesh was generated using `TetGen`[22] prescribing the maximal allowed volume of the tetrahedra. The resulting mesh $\mathcal{T}$ consisted of 106,983 volume elements. For some computations, also a uniform refinement $\mathcal{T}'$ was utilized, composed of 855,864 tetrahedra. Table 1 shows further mesh statistics, notably the maximum boundary layer height $y_{\max}$ and the area-weighted average boundary layer height $\bar{y}$, as defined by the height above each boundary face of the single adjacent tetrahedron.
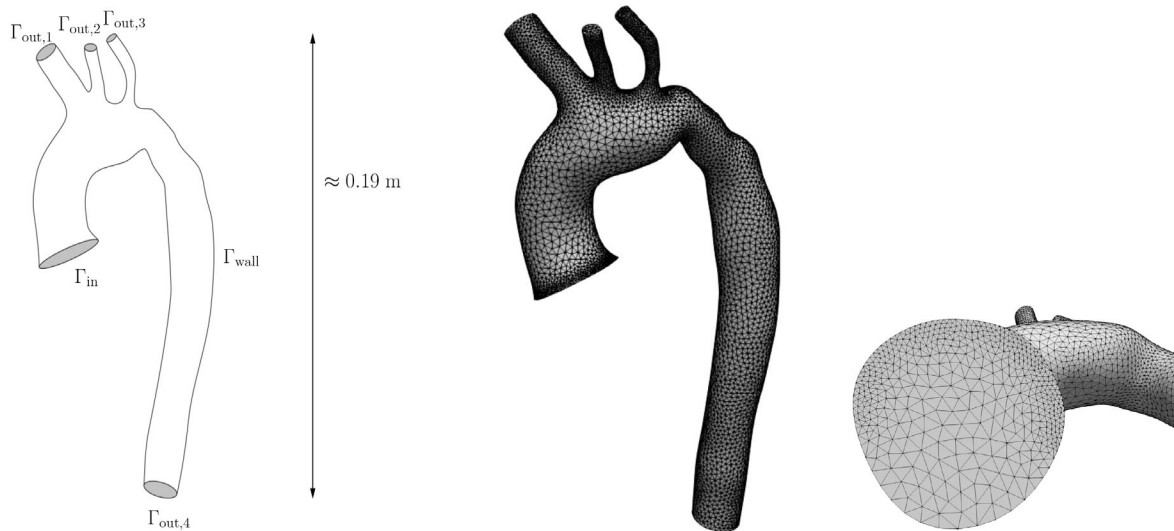

FIGURE 1   Left: Sketch of the computational domain, representing a segment of the aorta, and the corresponding decomposition of the boundary. Center and right: Surface mesh (coarser version), and zoom on the inlet boundary Γ_{in}.

TABLE 1   Mesh statistics: number of tetrahedra and vertices, maximum and average boundary layer height, maximum and average cell volume.

Mesh	Tetrahedra	Vertices	$y_{\max}$	$\bar{y}$	$V_{\max}$	$\overline{V}$
$\mathcal{T}$	106,983	21,495	3.8 mm	1.06 mm	43.2 mm^3	4.72 mm^3
$\mathcal{T}'$	855,864	158,335	2.18 mm	0.537 mm	5.39 mm^3	0.59 mm^3

On the one hand, the meshes were chosen to be fine in order to perform simulations with small spatial errors. But on the other hand, they were chosen to be sufficiently coarse in order to perform simulations in affordable computing times. Altogether, one encounters here a situation typical in practice, namely that any further (uniform) refinement of the meshes, which increases the computational costs at least by a factor of eight, is prohibitive from the point of view of computing times. It should be also noted that on the coarser mesh most turbulence models are applied with second-order finite elements for the velocity, so that the resolution in this respect corresponds to the mesh width of the fine mesh. Since most quantities of interest studied in this paper are based on the bulk flow, at different locations of the aorta segment, we decided to use rather uniform meshes for the whole domain, without special local adaptations.

Future studies may more closely investigate the sensitivity of quantities of interest to mesh refinement; however, due to the computational resources required and the complexity of comparing results computed with a broad variety of turbulence models on a broad variety of meshes this is out of the scope of this work.

In order to setup the numerical simulations, the patient-specific peak systolic velocity vector profiles measured using planar 4D VEC MRI were mapped onto the nodes of the meshed inlet boundary Γ_{in} using a linear interpolation scheme. The volume flow in the descending aorta was prescribed according to the MRI measurements. The flow difference between ascending and descending aorta was then distributed in the remaining outlets using the following assumptions: (i) the volume flow within the brachiocephalic artery (right arm and head) equals the volume flowing in both the left common carotid artery and left subclavian artery, and (ii) the flow distribution in the left common carotid artery and left subclavian artery depends on the cross-sectional areas of the outlets according to Murray's law, that is, $Q_i = \frac{D_i^3}{D_2^3 + D_3^3}$, where $i = 2$, 3, and Q_i stands for the flow rate in outlet $\Gamma_{\text{out},i}$. The resulting flow rates Q_i^*, $i = 1, ..., 4$, on the four outlet open boundaries (see Table 2) were used to define the lumped parameter models used as boundary conditions for the CFD simulation.

3 | METHODS

3.1 | Blood flow modeling

Let $\Omega \subset \mathbb{R}^3$ denote the computational domain and decompose its boundary $\partial\Omega$ as

$$\partial\Omega = \Gamma_{\text{in}} \cup \Gamma_{\text{wall}} \cup \Gamma_{\text{out},1} \cup ... \cup \Gamma_{\text{out},4},$$

(following the notation introduced in Figure 1, left). The inlet boundary Γ_{in} is situated close to the left ventricle, the arterial wall is denoted by Γ_{wall}, and $\Gamma_{\text{out},1}, ..., \Gamma_{\text{out},4}$ denote the artificial outlet boundaries created by cutting the physical domain and neglecting the downstream circulation.

In the considered physiological regime, the blood flow in Ω is modeled as an incompressible, Newtonian fluid, whose dynamics is described by the incompressible Navier–Stokes equations in terms of a velocity field $\boldsymbol{u}$ [m/s] : $\Omega \to \mathbb{R}^3$ and a pressure field p [Pa] : $\Omega \to \mathbb{R}$ satisfying the system of equations

$$\rho\partial_t\boldsymbol{u} - 2\mu\nabla \cdot \mathbb{D}(\boldsymbol{u}) + \rho(\boldsymbol{u} \cdot \nabla)\boldsymbol{u} + \nabla p = \boldsymbol{0} \text{ in } (0, T] \times \Omega,$$
$$\nabla \cdot \boldsymbol{u} = 0 \text{ in } (0, T] \times \Omega. \tag{1}$$

TABLE 2 Estimated flow rates and corresponding fraction of the inlet flow (absolute value) for each outlet (see also Figure 1, left) used in the simulations.

Boundary	Flow Q_i^* (m³/s)	Flow fraction out$_i$
$\Gamma_{\text{out},1}$ (brachiocephalic artery)	7.43×10^{-5}	16.81%
$\Gamma_{\text{out},2}$ (left common carotid artery)	3.80×10^{-5}	8.60%
$\Gamma_{\text{out},3}$ (left common subclavian artery)	3.63×10^{-5}	8.21%
$\Gamma_{\text{out},4}$ (descending aorta)	2.93×10^{-4}	66.38%
Inlet	4.42×10^{-4}	100.00%

In (1), T [s] is the final simulation time, $\rho = 1060\,\mathrm{kg/m^3}$ stands for the blood density, $\mu = 3.5 \times 10^{-3}\mathrm{Pa\,s}$ is the dynamic viscosity, and $\mathbb{D}(\boldsymbol{u}) = \left(\nabla\boldsymbol{u} + (\nabla\boldsymbol{u})^T\right)/2$ denotes the velocity deformation tensor (i.e., the symmetric part of the velocity gradient).

The characteristic peak velocity scale of the blood velocity in the ascending aorta is of the order of $U = \mathcal{O}(1)\,\mathrm{m/s}$. Using the diameter of the aorta $L = 0.03\,\mathrm{m}$ as characteristic length scale, the peak Reynolds number of the flow is

$$\mathrm{Re} = \frac{\rho L U}{\mu} \approx 9086,$$

which indicates a transition to turbulent flow.

For deriving the non-dimensional equations used in the numerical simulations, a characteristic length scale of $\widetilde{L} = 1\,\mathrm{m}$ was utilized, leading to the dimensionless viscosity coefficient

$$\nu = \frac{\mu}{\rho \widetilde{L} U} \approx 3.3 \cdot 10^{-6}.$$

Dividing (1) by ρ and using the dimensionless viscosity coefficient, the time-dependent incompressible Navier–Stokes equations can be written in fully dimensionless form:

$$\partial_t \boldsymbol{u} - 2\nu \nabla \cdot \mathbb{D}(\boldsymbol{u}) + (\boldsymbol{u} \cdot \nabla)\boldsymbol{u} + \nabla p = \boldsymbol{0} \text{ in } (0, T] \times \Omega,$$
$$\nabla \cdot \boldsymbol{u} = 0 \text{ in } (0, T] \times \Omega. \tag{2}$$

In what follows, with a slight abuse of notation, **u** and p will be used also to denote the (dimensionless) velocity and pressure fields.

3.1.1 | Initial and boundary conditions

The system of Equation (1) is completed by the following initial and boundary conditions, whose definition is motivated by the availability of data:

$$\begin{aligned}
\boldsymbol{u}(0, \boldsymbol{x}) &= \boldsymbol{0} & &\text{in } \Omega, \\
\boldsymbol{u}(t, \boldsymbol{x}) &= \boldsymbol{u}_{\mathrm{in}}(t, \boldsymbol{x}) := a(t)\boldsymbol{u}_{\mathrm{in}}^*(\boldsymbol{x}) & &\text{on } [0, T] \times \Gamma_{\mathrm{in}}, \\
\boldsymbol{u}(t, \boldsymbol{x}) &= \boldsymbol{0} & &\text{on } [0, T] \times \Gamma_{\mathrm{wall}}, \\
2\mu\mathbb{D}(\boldsymbol{u})\boldsymbol{n} - p\boldsymbol{n} &= -P_i(\boldsymbol{u})\boldsymbol{n} & &\text{on } [0, T] \times \Gamma_{\mathrm{out},i}, \ i = 1, ..., 4.
\end{aligned} \tag{3}$$

In Equation (3)-2, $\boldsymbol{u}_{\mathrm{in}}^*$ [m/[s]] $: \Gamma_{\mathrm{in}} \to \mathbb{R}^3$ is the inlet velocity vector profile derived from MRI measurements as described above and $a : \mathbb{R} \to \mathbb{R}$ is an artificial smooth function such that $a(0) = 0$ and which becomes periodic with period $T_0 = 1\,\mathrm{s}$ after a given time $t_0 = 0.01\,\mathrm{s}$, that is, $a(t + T_0) = a(t)$, for all $t > t_0$ (see Figure 2). Equation (3)-3 models the arterial wall as rigid, while the Neumann boundary conditions (3)-4 are imposed via lumped parameter models $P_i(\boldsymbol{u})$, $i = 1, ..., 4$, which shall be defined in order to obtain a simulation setup in agreement with the measured outlet flow rates.

The selection of the boundary conditions at the outlets has to take into account the amount of available data. Since only outflow measurements at systole are at hand, one has to choose a model whose parameters can be determined with these data. The boundary conditions on the outlets are thus defined by the purely resistive model

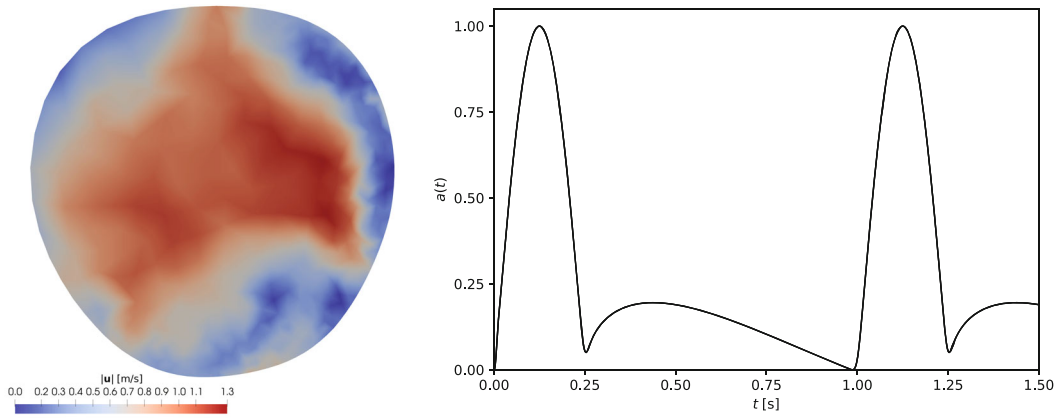$$P_i(t) = R_i Q_i(t), \quad i = 1, ..., 4, \tag{4}$$

where

FIGURE 2 Left: Magnitude plot of the measured inlet velocity profile, oriented such that the view is up into the ascending aorta. The aortic arch curves away in a "downward" direction relative to the page. Right: The inflow pulse profile $a(t)$ plotted over the first 1.5 seconds.

$$Q_i := \int_{\Gamma_{\text{out},i}} \boldsymbol{u} \cdot \boldsymbol{n} \; d\boldsymbol{s},$$

for $i = 1, \ldots, 4$, denotes the outgoing flow through the outlet $\Gamma_{\text{out},i}$. The iterative approach for defining the boundary resistances will be discussed in more detail in Section 3.3.

> *Remark* 1. Model (4) does not take into account more complex interactions with the downstream circulation; an obvious option would be a Windkessel model with 3 or 4 elements. However, increasing the model complexity requires additional parameters and assumptions, which cannot realistically be adjusted to a patient-specific context without additional data.

3.1.2 | Outflow stabilization

It is well known that blood flow simulations of aortic flow might be affected by backflow instabilities, i.e., spurious oscillations at the open boundaries, when the flow is directed "back" into the computational domain.[23] To overcome this issue, a directional do-nothing condition[24,25] is considered, which can be seen as a modification of the Neumann boundary conditions (3)-3 of the form

$$(2\mu\mathbb{D}(\boldsymbol{u}) - pI)\boldsymbol{n} = -P_i(t)\boldsymbol{n} + \frac{\beta}{2}(\boldsymbol{u} \cdot \boldsymbol{n})_{-}\boldsymbol{u} \text{ on } [0,T] \times \Gamma_{\text{out},i},$$

$i = 1, \ldots, 4$, where $(\boldsymbol{u} \cdot \boldsymbol{n})_{-} = \min\{\boldsymbol{u} \cdot \boldsymbol{n}, 0\}$ is the negative part of the boundary velocity's normal component and $\beta \geq 0$ is a scaling parameter. In our simulations, $\beta = 1$. This approach has been extensively used in computational hemodynamics[26,27] and has been shown to be a natural means to control a priori energy estimates[25] for $\beta = 1$. Alternative backflow stabilization approaches have been recently proposed, considering, among others, tangential regularization of the boundary flow,[28] stabilization based on the residue of a surrogate Stokes problem,[29] or on a rotational velocity correction.[30] The interested reader is referred to a benchmark study[23] and the references therein.

3.2 | Spatial and temporal discretizations

The system of Equations (2) is discretized in space using a finite element method. In order to introduce the formulation, let $\mathcal{T}_h$ denote the considered regular tetrahedral mesh, let h be its characteristic size, and let $\boldsymbol{V}_h$ and Q_h denote continuous piecewise polynomial spaces defined on $\mathcal{T}_h$. Furthermore, let

$$V_{h,0} = \{v_h \in V_h : v_h \equiv 0 \text{ on } \Gamma_{\text{in}} \cup \Gamma_{\text{wall}}\}$$

be the subspace of V_h including the essential boundary conditions on the inlet boundary and the arterial wall.

Let us introduce the nonlinear form

$$\text{Gal}((u_h, p_h), (v_h, q_h)) := \nu a(u_h, v_h) + b(u_h; u_h, v_h) - (\nabla \cdot v_h, p_h) + (\nabla \cdot u_h, q_h) - f(u_h, v_h)$$

with

$$a(u_h, v_h) := 2(\mathbb{D}(u_h), \mathbb{D}(v_h)), \quad b(u_h; v_h, w_h) := ((u_h \cdot \nabla)v_h, w_h),$$

and

$$f(u_h, v_h) := \sum_{i=1}^{4} \left(P_i(u_h)n + \frac{1}{2}(u_h \cdot n)_{-} u_h, v_h \right)_{\Gamma_{\text{out},i}}.$$

The standard Galerkin discrete formulation of (2) reads: Find $(u_h, p_h) : [0, T] \to V_h \times Q_h$ such that $u_h \equiv 0$ on $[0, T] \times \Gamma_{\text{wall}}$, u_h satisfies $(3)_1$, and

$$(\partial_t u_h, v_h) = -\text{Gal}((u_h, p_h), (v_h, q_h)) \tag{5}$$

for all $t \in (0, T)$ and for all $(v_h, q_h) \in V_{h,0} \times Q_h$.

Equation (5) is discretized in time using a BDF-2 scheme, an A-stable second-order method that has the advantage of requiring residuals of only one time step:

$$\left(u_h(t_n) - \frac{4}{3}u_h(t_{n-1}) + \frac{1}{3}u_h(t_{n-2}) \right) + \frac{2}{3}\Delta t\,\text{Gal}((u_h, p_h), (v_h, q_h)) = 0. \tag{6}$$

Since the scheme requires the solution at two previous time instants, the first time iteration is performed using a backward Euler method:

$$(u_h(t_n) - u_h(t_{n-1})) + \Delta t\,\text{Gal}((u_h, p_h), (v_h, q_h)) = 0. \tag{7}$$

At each time step, a nonlinear problem in the velocity and pressure has to be solved. This is handled via a Picard method. Namely, the convective term $b(u_h; u_h, v_h)$ and the boundary condition term $f(u_h, v_h)$ in (5) are linearized using the velocity field $\hat{u}_h$ computed at the last iteration, thus resulting in a linear system with the following linearization of the Galerkin term at each Picard iteration

$$\widehat{\text{Gal}}\left(\hat{u}_h^b, \hat{u}_h^f; (u_h, p_h), (v_h, q_h) \right) = \nu a(u_h, v_h) + b\left(\hat{u}_h^b; u_h, v_h \right) - (\nabla \cdot v_h, p_h) + (\nabla \cdot u_h, q_h) - f\left(\hat{u}_h^f, v_h \right), \tag{8}$$

where the solution (u_h, p_h) denotes the next iterate. This form depends on the previous Picard iteration's results or, in the first iteration, the initial guess. We have avoided marking this dependence in the notation or introducing iteration indices, for brevity's sake. The linearized form $\widehat{\text{Gal}}$—in practice, one of the modified forms $\widehat{\text{Gal}}_{\text{Sma}}$ or $\widehat{\text{Gal}}_{\text{RB}}$ introduced in Section 3.4—is then substituted for Gal in (6) and (7) to arrive at the linear problem for each Picard iteration. The initial guess is provided by linear extrapolation from the previous two time steps.

The linear problems to be solved in each Picard iteration have a saddle point structure. As will be shown in Section 3.4, the same structure is retained for each considered turbulence model, with the exception of the RB-VMS model discussed in Section 3.4.4.

3.3 | Estimation of boundary resistances

The outlet resistances R_i, $i = 1, ..., 4$, were tuned in order to obtain simulated outflow rates Q_i at systole close to the measured reference values Q_i^* given in Table 2. To this purpose, a sequential estimation approach was implemented, in which the parameter values are optimized during the time iteration depending on the difference between simulated values and available data.

The approach is motivated by two observations. Firstly, considering a surrogate 0D model of the downstream circulation, the systemic vascular resistance (SVR), the resistance to blood flow offered by all of the systemic vasculature excluding the pulmonary tract and the small resistance of the upper aorta itself, can be defined by the relation

$$R_{SV} = \left(\sum_{i=1}^{4} R_i^{-1}\right)^{-1} = \left(\sum_{i=1}^{4} G_i\right)^{-1}, \tag{9}$$

where $G_i := R_i^{-1}$ denote the outlet conductances. Secondly, mass conservation guarantees

$$\sum_{i=1}^{4} Q_i(t) = \sum_{i=1}^{4} Q_i^* = Q_{in}. \tag{10}$$

On the one hand, mass conservation implies therefore that the four available measurements are not independent. On the other hand, if the inlet flow is constant in time, one obtains

$$\sum_{i=1}^{4} \dot{Q}_i(t) = 0. \tag{11}$$

For a given value of the systemic vascular resistance R_{SV},[a] the parameter estimation method is based on the solution of a Navier–Stokes problem

$$\begin{aligned}
\rho \partial_t \boldsymbol{u} - 2\mu \nabla \cdot \mathbb{D}(\boldsymbol{u}) + \rho(\boldsymbol{u} \cdot \nabla)\boldsymbol{u} + \nabla p &= \boldsymbol{0} &&\text{in } (0, T] \times \Omega, \\
\nabla \cdot \boldsymbol{u} &= 0 &&\text{in } (0, T] \times \Omega \\
\boldsymbol{u}(t, \boldsymbol{x}) = \boldsymbol{u}_{in}(t, \boldsymbol{x}) &= \widehat{a}(t)\boldsymbol{u}_{in}^*(\boldsymbol{x}), &&\text{for } (t, \boldsymbol{x}) \in [0, T] \times \Gamma_{in}, \\
2\mu \mathbb{D}(\boldsymbol{u})\boldsymbol{n} - p\boldsymbol{n} &= -G_i(t)^{-1}Q_i(t)\boldsymbol{n} &&\text{on } [0, T] \times \Gamma_{out,i}, \; i = 1, ..., 4, \\
\boldsymbol{u}(0, \boldsymbol{x}) &= \boldsymbol{u}_0(\boldsymbol{x}) &&\text{in } \Omega,
\end{aligned} \tag{12}$$

coupled to an additional ODE for the conductances:

$$\dot{G}_i(t) = \frac{\gamma_0}{Q_{in}}\left(Q_i^* - Q_i(t)\right), \quad G_i(0) = G_i^0, \; i = 1, ..., 4, \tag{13}$$

and with the additional condition (9), that is,

$$\sum_{i=1}^{4} G_i^0 = R_{SV}^{-1}. \tag{14}$$

Equation (14) is imposed in order to overcome the dependency of the outlet measurements stated in (10). In (12), the function $\widehat{a}(t)$ defines a smooth transition to a constant profile, that is, it is such that $\widehat{a}(0) = 0$, $d_t\widehat{a}(0) = 0$, and $\widehat{a}(t) = 1$ for all $t > t_1 = 0.05$ s. In particular, it follows from (11) that, when the inflow is constant (for $t > t_1$), the sum of conductances also remains constant over time. In (13), γ_0 is a positive parameter and the initial values of G_i^0 can be obtained, for example, by successive simulations with decreasing viscosity.

If the system (12)-(13) reaches a steady state, then $Q_i^* = Q_i(t)$ for $i = 1,...,4$, and the corresponding stationary values of $R_i = G_i^{-1}$, $i = 1,...,4$, can be used for the blood flow simulation. In practice, due to the presence of turbulence, the values for the resistances are defined taking a suitable long-term average of the solution once a quasi-periodic state has been reached.

Once the outlet resistances $R_i = R_i^*(R_{SV})$ have been determined for a certain R_{SV} solving (12)–(14), the values $R_i' = R_i^*(R_{SV}')$ for a different systemic vascular resistance R_{SV}' have been computed considering that the difference between R_{SV} and R_{SV}' induces a shift in the overall blood pressure in Ω. Namely, let us denote by $(\boldsymbol{u}, p)$ and G_1, G_4 the solutions to (12), (13), and (14). Then, there exists a constant ΔP such that $(\boldsymbol{u}, p + \Delta P)$ satisfies (12) at the steady state with $G_i' = (R_i')^{-1}$, and

$$R_i' = R_i + \frac{\Delta P}{Q_i^*}, \quad i = 1,,4,$$

that is, such that the pressure at each outlet increases by ΔP when $Q_i = Q_i^*$. Hence, the value of ΔP can be computed from Equation (14) as a function of R_{SV}' solving

$$\frac{1}{R_{SV}'} = \sum_{i=1}^4 \frac{1}{R_i'} = \sum_{i=1}^4 \frac{1}{R_i + \frac{\Delta P}{Q_i^*}}. \tag{15}$$

It can be shown that R_{SV}' in (15) is a smooth and monotonous function of ΔP, for $\Delta P > -\min_i Q_i^* R_i$. Moreover, since

$$R_{SV}'(\Delta P) \to \infty \text{ for } \Delta P \to \infty \quad \text{and} \quad R_{SV}'(\Delta P) \to 0 \text{ for } \Delta P \to -\min_i Q_i^* R_i,$$

one can conclude that there exists a unique ΔP that satisfies (15) for a given R_{SV}', or, equivalently, such that $R_i' Q_i^* = Q_i^* R_i + \Delta P$ for all outlets.

In practice, the approach delivered satisfactory results for moderate values of γ_0 (see Section 4.1 for more details) and with a negligible influence of the discretization used. However, rigorous convergence estimates are out of the scope of this work.

> Remark 3. *Average blood pressure.* Prescribing the systemic vascular resistance is equivalent to fixing the pressure constant for the solution of the Navier–Stokes problem (12). In fact, since $(\boldsymbol{u}, p + \Delta P)$ satisfies (12) for the new value of the systemic vascular resistance, ΔP in Equation (15) determines also the shift in the average blood pressure in the considered aortic segment.

3.4 | Turbulence modeling

This section provides a brief presentation of the turbulence models that were investigated in the numerical studies. Turbulence models augment the Galerkin discretization with additional terms that model the impact of the subgrid scales onto the resolved scales. From the numerical point of view, a turbulence model serves as a stabilization by introducing in some sophisticated way numerical viscosity, which is obvious for the eddy viscosity models described below and the stabilizing effect of the RB-VMS model is explained, for example, in Bazilevs et al.[18] and Ahmed et al.[31]

3.4.1 | The Smagorinsky model

The Smagorinsky model[13] is certainly one of the most popular LES models, but also one of the simplest. The model relies on the Boussinesq hypothesis that the effect of small-scale fluctuations on large-scale flow behavior is mostly dissipative. Motivated by this assumption, the deviatoric part of the subgrid-scale (SGS) stress tensor τ,

$$\tau_{ij} = \overline{u_i u_j} - \overline{u}_i \overline{u}_j,$$

is modeled by a nonlinear scalar multiple of the velocity deformation tensor $\mathbb{D}(\boldsymbol{u})$, that is,

$$\tau_{ij} \approx -2\nu_t \mathbb{D}(\boldsymbol{u})_{ij} + \delta_{ij} \frac{\text{trace}(\tau)}{3}, \tag{16}$$

with a suitable turbulent or eddy viscosity $\nu_t = \nu_t(\boldsymbol{u})$. Equation (16) results in an additional nonlinear viscous term in the momentum balance of the Navier–Stokes equations (1), which has the form

$$-2\nu_t \nabla \cdot \mathbb{D}(\boldsymbol{u}),$$

while the trace part of the SGS stress tensor is hidden in the modified filtered pressure

$$\widetilde{p} = p + \frac{\text{trace}(\tau)}{3},$$

requiring no further modification of (1).

In the semidiscrete formulation (5), the Smagorinsky model amounts to adding the term $-(\nu_t \mathbb{D}(\boldsymbol{u}_h), \mathbb{D}(\boldsymbol{v}_h))$ to the right-hand side. Linearization for the Picard iteration is achieved by computing ν_t from the current iterate $\widehat{\boldsymbol{u}}_h$, resulting in the adjusted bilinear form

$$\widehat{\text{Gal}}_{\text{Sma}}((\boldsymbol{u}_h, p_h), (\boldsymbol{v}_h, q_h)) = \widehat{\text{Gal}}\left(\widehat{\boldsymbol{u}}_h, \widehat{\boldsymbol{u}}_h^0; (\boldsymbol{u}_h, p_h), (\boldsymbol{v}_h, q_h)\right) + (\nu_t(\nabla \widehat{\boldsymbol{u}}_h) \mathbb{D}(\boldsymbol{u}_h), \mathbb{D}(\boldsymbol{v}_h)) \tag{17}$$

with the Galerkin terms $\widehat{\text{Gal}}$ described in (8). Here the convective term b is linearized using the previous Picard iterate (or initial guess) $\widehat{\boldsymbol{u}}_h$, whereas the boundary term f is computed at the beginning of the iteration from the initial guess $\widehat{\boldsymbol{u}}_h^0$.

The Smagorinsky model uses dimensional arguments at Kolmogorov scales to arrive at the Smagorinsky eddy viscosity

$$\nu_t = C_{\text{Sma}} \delta^2 \| \mathbb{D}(\boldsymbol{u}) \|_{\text{F}}. \tag{18}$$

In (18), $\| \mathbb{D}(\boldsymbol{u}) \|_{\text{F}}$ is the Frobenius norm of the velocity deformation tensor, δ is a local length scale, and C_{Sma} is a user-chosen constant. The advantages and drawbacks of the Smagorinsky model for practical simulations are well known (Reference 32, chapter 5.3). From the mathematical point of view, concerning questions such as existence and uniqueness of a weak solution and finite element error analysis, the Smagorinsky model belongs to the best-understood turbulence models (Reference 33, chapter 8.3).

For the simulations presented in this paper, the local length scale was chosen to be piecewise constant on each mesh element, that is, $\delta = 2h_{K,\text{sh}}$, where $h_{K,\text{sh}}$ is the length of the shortest edge of mesh cell K. This choice of δ proportional to the shortest edge has been proven to be better than other approaches, e.g. using the diameter of the cell.[34] The constant C_{Sma} is a free parameter of the model. Different values $C_{\text{Sma}} \in \{0.01, 0.005\}$ were investigated in our simulations. These values have been proven to be appropriate ones in benchmark problems for incompressible turbulent flow simulations (Reference 33, chapter 8.9).

3.4.2 | The Vreman model

The Vreman model[14] proposes an alternate eddy viscosity. It is motivated by the Smagorinsky model's excessively dissipative behavior in laminar and transitional flows, including shear flows near walls. Using algebraic arguments, involving the classification of local flow behaviors for which the subgrid dissipation

$$D_\tau = -\tau : \nabla \boldsymbol{u}$$

vanishes compared to various functionals of the velocity gradient field, the following form of eddy viscosity is considered:

$$\nu_t = \frac{C_{\mathrm{Vre}}}{\|\nabla \boldsymbol{u}\|_F} \sqrt{B_\beta}. \tag{19}$$

In (19), $\|\nabla \boldsymbol{u}\|_F$ is the Frobenius norm of the velocity gradient, C_{Vre} is a free parameter, and

$$B_\beta = \frac{1}{2} \sum_{i,j=1}^3 \left(\beta_{ii}\beta_{jj} - \beta_{ij}^2 \right) = \sum_{1 \le i < j \le 3} \left(\beta_{ii}\beta_{jj} - \beta_{ij}^2 \right),$$

where

$$\beta_{ij} = \sum_{k=1}^3 \delta_k^2 \partial_k u_i \partial_k u_j,$$

is a rotational invariant of the symmetric positive definite tensor $\beta = \nabla \boldsymbol{u} \delta^2 (\nabla \boldsymbol{u})^T$ with anisotropic filter widths

$$\delta = \begin{pmatrix} \delta_1 & 0 & 0 \\ 0 & \delta_2 & 0 \\ 0 & 0 & \delta_3 \end{pmatrix}.$$

Note that if β has eigenvalues $\lambda_1, \lambda_2, \lambda_3$, then

$$B_\beta = \lambda_1\lambda_2 + \lambda_1\lambda_3 + \lambda_2\lambda_3.$$

The k-th length scale δ_k is again chosen piecewise constant. On each mesh cell K, $\delta_k = \delta_k(K)$ is the width of K in the k-th coordinate direction:

$$\delta_k(K) = \max_{\boldsymbol{x},\boldsymbol{x}' \in K} |x_k - x_k'|.$$

In regions where $\nabla \boldsymbol{u}$ is (nearly) zero, the eddy viscosity is taken to be zero. This choice is consistent: $|\beta| \lesssim \|\nabla \boldsymbol{u}\|^2$, so $\sqrt{B_\beta} \lesssim \sqrt{|\beta|^2} \lesssim \|\nabla \boldsymbol{u}\|^2$ and $\nu_t \lesssim \|\nabla \boldsymbol{u}\|$, as in the Smagorinsky model.

Using the Vreman model, the flow in the considered segment of the aorta was simulated with $C_{\mathrm{Vre}} = 0.07$, that is, the value suggested by Vreman[14] based on scaling arguments.

As with the Smagorinsky model, we linearize using the previous iterate, again arriving at (17).

3.4.3 | The σ-model

The σ-model[15], developed by Nicoud et al., is an eddy viscosity model motivated by similar arguments as those used for the Vreman model, namely the prevention of spurious artificial dissipation in certain flow configurations. To this purpose, the model postulates an eddy viscosity of the form

$$\nu_t = (C_\sigma \delta)^2 \mathcal{D}_\sigma,$$

where δ is the filter width, C_σ is a scaling parameter, and $\mathcal{D}_\sigma = \mathcal{D}_\sigma(\nabla \boldsymbol{u})$ is a nonlinear differential operator which satisfies the following properties:

P0: $\mathcal{D}_\sigma \geq 0$, that is, no negative viscosity and no additional filtering steps,

P1: cubic behavior near solid boundaries, that is, $\mathcal{D}_\sigma \sim y^3$ near $y = 0$ for shear flows above the xz-plane,

P2: $\mathcal{D}_\sigma = 0$ for less than three-dimensional flows, that is, when $\mathrm{rank}(\nabla \boldsymbol{u}) \leq 2$,

P3: $\mathcal{D}_\sigma = 0$ for axisymmetric (and, in the case of compressible flows, isotropic) expansion or contraction,

*P4: $\mathcal{D}_\sigma$ should scale with frequency, that is, $\mathcal{D}_\sigma(\lambda \mathbf{g}) = |\lambda| \mathcal{D}_\sigma(\mathbf{g})$.

These requirements are justified largely by arguments from experimental observation and engineering constraints. The σ-model satisfies them by taking

$$\mathcal{D}_\sigma(\nabla \boldsymbol{u}) = \frac{\sigma_3(\sigma_1 - \sigma_2)(\sigma_2 - \sigma_3)}{\sigma_1^2},$$

where $\sigma_1 \geq \sigma_2 \geq \sigma_3 \geq 0$ are the singular values of $\nabla \boldsymbol{u}$, taking $\mathcal{D}_\sigma(\mathbf{0}) = 0$. This choice fulfills **P0** by the ordering of the singular values, **P2** and **P3** by the product in the numerator, and ***P4** by the scale factor σ_1^{-2}; **P1** is justified using Taylor expansion near $y = 0$ (Reference 15, section II.B).

In the numerical simulation, the value $C_\sigma = 1.35$ was used, as obtained by Nicoud et al. (Reference 15, section III) using both a simple randomized procedure and a dynamic tuning approach applied to a high-fidelity decaying isotropic turbulence simulation.

Apart from the computation of ν_t, the σ-model functions the same way as the previous eddy viscosity models and is linearized as in (17).

3.4.4 | The RB-VMS model

The last considered turbulence model is the residual-based variational multiscale (RB-VMS) approach proposed by Bazilevs et al.[18] The major conceptual difference with respect to the eddy viscosity LES models (Sections 3.4.1–3.4.3) lies in how the scale separation is achieved. LES models typically proceed from the notion of applying a convolutional low-pass filter to the Navier–Stokes equations (1), exchanging convolution and differentiation, and modeling the remaining term involving the SGS stress tensor. Variational multiscale models are instead based on a decomposition of both the velocity and pressure spaces of the Navier–Stokes problem's variational form into two or more "coarse" and "fine" spaces.

The RB-VMS model is a two-scale model.[31] In the context of a finite element method for discretizing the variational problem, the coarse scales are defined as those resolved by the finite element discretization, while the fine scales are the remaining (unresolved) ones.

Let $(\boldsymbol{u}, p) = (\boldsymbol{u}_h, p_h) + (\boldsymbol{u}', p')$ denote the decomposition into coarse and fine scales and let $\mathrm{Res}(\boldsymbol{u}_h, p_h) = (\boldsymbol{r}_m, r_c)$ denote the (pointwise) residual of the coarse solution. Following Bazilevs et al.,[18] the major modeling assumptions behind RB-VMS are (i) a representation of the fine-scale components by a truncated perturbation series of $\varepsilon = \| \mathrm{Res}(\boldsymbol{u}_h, p_h) \|$, i.e.,

$$(\boldsymbol{u}', p') = \sum_{k \geq 1} \varepsilon^k (\mathbf{u}'_k, p'_k) \approx \varepsilon(\mathbf{u}'_1, p'_1),$$

and (ii) an approximation of the fine-scale Green's operator relating $(\boldsymbol{u}'_k, p'_k)$ to $(\boldsymbol{u}'_1, p'_1)$, ..., $(\boldsymbol{u}'_{k-1}, p'_{k-1})$ and $\mathrm{Res}(\boldsymbol{u}_h, p_h)$ by a 4×4 diagonal tensor

$$\tau = \begin{pmatrix} \tau_m \mathbb{I}_3 & 0 \\ 0 & \tau_c \end{pmatrix}$$

times a Dirac distribution, with momentum and continuity stabilization parameters τ_m and τ_c, which will be discussed in more detail below. The model for the fine scales then reads

$$
\begin{aligned}
\boldsymbol{u}' &\approx -\tau_m \boldsymbol{r}_m(\boldsymbol{u}_h, p_h) = -\tau_m(\partial_t \boldsymbol{u}_h + (\boldsymbol{u}_h \cdot \nabla)\boldsymbol{u}_h + \nabla p_h - \nu \Delta \boldsymbol{u}_h), \\
p' &\approx -\tau_c r_c(\boldsymbol{u}_h) = -\tau_c(\nabla \cdot \boldsymbol{u}_h).
\end{aligned}
$$

Note that $\Delta \boldsymbol{u}_h$ is typically not well-defined in terms of pointwise or weak derivatives of $\boldsymbol{u}_h$ in Ω, as $\boldsymbol{u}_h$ is only continuous piecewise polynomial. In our numerical simulations, pointwise second derivatives on the interior of each tetrahedral cell are used, but projection-based methods of dealing with this term may also be explored (Reference 18, page 181).

Finally, by considering interactions between fine and coarse scales (with a few additional assumptions[b]) and using integration by parts to avoid derivatives of the residuals, the following modified semi-discrete problem is obtained:

Find $(\boldsymbol{u}_h, p_h) : [0, T] \to \boldsymbol{V}_h \times Q_h$ such that

$$
\begin{aligned}
(\partial_t \boldsymbol{u}_h, \boldsymbol{v}_h) = &-\text{Gal}((\boldsymbol{u}_h, p_h), (\boldsymbol{v}_h, q_h)) - \tau_m(\boldsymbol{r}_m(\boldsymbol{u}_h, p_h), (\boldsymbol{u}_h \cdot \nabla)\boldsymbol{v}_h) - \tau_m(\boldsymbol{r}_m(\boldsymbol{u}_h, p_h), \nabla q_h) \\
&-\tau_c(r_c(\boldsymbol{u}_h), \nabla \cdot \boldsymbol{v}_h) - \tau_m\left(\boldsymbol{r}_m(\boldsymbol{u}_h, p_h), (\nabla \boldsymbol{v}_h)^T \boldsymbol{u}_h\right) + \tau_m^2\left(\boldsymbol{r}_m(\boldsymbol{u}_h, p_h) \bigotimes \boldsymbol{r}_m(\boldsymbol{u}_h, p_h), \nabla \boldsymbol{v}_h\right)
\end{aligned}
\tag{20}
$$

at all times $t \in (0, T]$ and for all $\boldsymbol{v}_h \in \boldsymbol{V}_{h,0}$, $q_h \in Q_h$. In (20), $\text{Gal}(\cdot, \cdot)$ denotes the terms resulting from the Galerkin discretization of (1) as in (5), and the remaining terms result from cross stresses (i.e., the interactions between coarse and fine scales) and, in the case of the last term, SGS stresses (i.e., fine-fine interactions).

Note that, except for the grad-div term $\tau_c(r_c(\boldsymbol{u}_h), \nabla \cdot \boldsymbol{v}_h)$, all the additional terms introduced by the RB-VMS model are at least quadratic in $\boldsymbol{u}_h$, and the SGS term is quadratic in p_h. As a consequence, different approaches are possible when linearizing the problem for a Picard iteration scheme.

Let $(\widehat{\boldsymbol{u}}_h, \widehat{p}_h)$ denote the initial guess or last Picard iterate. The stabilization parameters τ_m, τ_c may depend on $\boldsymbol{u}_h$. In this case they are computed from $\widehat{\boldsymbol{u}}_h$. For legibility, this dependency will not be marked in the notation. Linearizing the term $\boldsymbol{r}_m$ as

$$
\widehat{\boldsymbol{r}}_m(\boldsymbol{u}_h, p_h) = \partial_t \boldsymbol{u}_h + (\widehat{\boldsymbol{u}}_h \cdot \nabla)\boldsymbol{u}_h + \nabla p_h - \nu \Delta \boldsymbol{u}_h,
$$

one obtains the modified bilinear form:

$$
\begin{aligned}
\widehat{\text{Gal}}_{\text{RB}}((\boldsymbol{u}_h, p_h), (\boldsymbol{v}_h, q_h)) = &\widehat{\text{Gal}}(\widehat{\boldsymbol{u}}_h, \widehat{\boldsymbol{u}}_h; (\boldsymbol{u}_h, p_h), (\boldsymbol{v}_h, q_h)) + \tau_m(\widehat{\boldsymbol{r}}_m(\boldsymbol{u}_h, p_h), (\widehat{\boldsymbol{u}}_h \cdot \nabla)\boldsymbol{v}_h) + \tau_m(\widehat{\boldsymbol{r}}_m(\boldsymbol{u}_h, p_h), \nabla q_h) \\
&+\tau_c(r_c(\boldsymbol{u}_h), \nabla \cdot \boldsymbol{v}_h) + \tau_m\left(\widehat{\boldsymbol{r}}_m(\boldsymbol{u}_h, p_h), (\nabla \boldsymbol{v}_h)^T \widehat{\boldsymbol{u}}_h\right) - \tau_m^2\left(\widehat{\boldsymbol{r}}_m(\widehat{\boldsymbol{u}}_h, \widehat{p}_h) \bigotimes \widehat{\boldsymbol{r}}_m(\boldsymbol{u}_h, p_h), \nabla \boldsymbol{v}_h\right),
\end{aligned}
$$

where $\widehat{\text{Gal}}(\cdot, \cdot)$ denotes the linearization of the Galerkin terms, as in (8). Here both the convective term b and the boundary term f are computed at each Picard iteration from the previous iterate $\widehat{\boldsymbol{u}}_h$. The momentum residual $\boldsymbol{r}_m$ (and the linearized version $\widehat{\boldsymbol{r}}_m$) depend on time derivatives of the velocity. This dependency is addressed by shifting terms involving $\partial_t \boldsymbol{u}_h$ to the time discretization's modified mass matrix and discretizing $\partial_t \widehat{\boldsymbol{u}}_h$ as

$$
\partial_t \widehat{\boldsymbol{u}}_h \approx \frac{1}{\Delta t}\left(\widehat{\boldsymbol{u}}_h - \boldsymbol{u}_{h,\text{prev}}\right),
$$

where $\boldsymbol{u}_{h,\text{prev}}$ is the previous time step's velocity.

Bazilevs et al.[18] (Equations 63 and 64) suggest the following formulas for τ_m and τ_c for equal-order pairs, based on asymptotic scaling arguments for stabilized finite element methods:

$$
\tau_m(K, \boldsymbol{u}_h) = \left(\frac{4}{\Delta t^2} + \boldsymbol{u}_h \cdot \boldsymbol{G}\boldsymbol{u}_h + C_I \nu^2 (\boldsymbol{G} : \boldsymbol{G})\right)^{-\frac{1}{2}}, \quad \tau_c(K, \boldsymbol{u}_h) = \frac{1}{\tau_m(K, \boldsymbol{u}_h)|\boldsymbol{g}|^2},
\tag{21}
$$

In (21), K denotes a cell of the finite element mesh, $\boldsymbol{G} = (\nabla \boldsymbol{F}^{-1})^T \nabla \boldsymbol{F}^{-1}$ and $\boldsymbol{g} = {}^T \nabla \boldsymbol{F}^{-1}$ are derived from the local reference transformation $\boldsymbol{F}^{-1} : K \rightarrow \widehat{K}$, and C_I is the constant of an element-wise inverse estimate. This inverse estimate is not clearly specified and, in general, not trivial to obtain. However, as the C_I term scales with ν^2, its influence can be assumed to be negligible in a highly turbulent situation. For our computations with equal-order pairs, we used $C_I = 1$.

Using inf-sup stable pairs, the stabilization parameters were defined as

$$\tau_m = \max\left(\delta_0 h_{K,\text{sh}}^2, \frac{\Delta t}{2}\right), \quad \tau_c = \delta_1$$

with scaling parameters δ_0, δ_1 and the local cell's shortest edge length $h_{K,\text{sh}}$. In the numerical simulation, the values $\delta_0 = 1$, $\delta_1 = 0.25$ were chosen.

3.5 | Simulation setup

Numerical simulations with the three eddy viscosity models described in Sections 3.4.1, 3.4.2, and 3.4.3 were run using inf-sup stable Taylor–Hood finite elements, that is, continuous piecewise quadratic velocities ($\boldsymbol{V}_h = \mathrm{P}_2(\mathcal{T})^3$) and continuous piecewise linear pressures ($Q_h = \mathrm{P}_1(\mathcal{T})$). This pair of spaces is probably the most popular inf-sup stable pair. The RB-VMS model (Section 3.4.4) includes a stabilizing pressure–pressure term and therefore does not necessarily require inf-sup stable finite element spaces. In this case, results using $\mathrm{P}_2^3 \times \mathrm{P}_1 =: \mathrm{P}_2/\mathrm{P}_1$ elements on $\mathcal{T}$ were also compared to those obtained with equal-order $\mathrm{P}_1/\mathrm{P}_1$ elements on $\mathcal{T}$ and on a refinement $\mathcal{T}'$. Table 3 provides information on the dimensions of the resulting discrete problems depending on the different choices for the discretization for the two computational meshes.

The time discretization was based on a BDF-2 scheme with a fixed time step length of $\Delta t = 1/8 \times 10^{-3}$s. This time step was determined in preliminary studies to be appropriate in the sense that it is sufficiently fine that moderate variation has negligible impact on the quantities of interest and sufficiently large for performing simulations in reasonable time. In particular, it is of the same order of magnitude as the time step proposed by Lancellotti et al.[35] for direct numerical simulations of blood flows in realistic stenotic carotids, there obtained by estimating the maximum frequency of perturbation modes of a simplified shear layer instability model.

The resulting nonlinear systems were solved using a Picard iteration, stopping the iteration when the Euclidean norm of the residual vector was less than or equal to 10^{-10}. This was usually achieved in one or two iterations. The corresponding linear systems were solved by a flexible GMRES iteration, using a least-squares commutator preconditioner[c][36] for the eddy viscosity models, which has previously performed very efficiently in numerical studies,[37] and a hybrid FGMRES/BiCGSTAB approach[d] for the RB-VMS models.

> *Remark* 4. *Preconditioning.* Since the RB-VMS method includes a pressure–pressure coupling term, the system matrix always includes a nonzero pressure–pressure block, rendering classical saddle point solvers or preconditioners inapplicable. Although there exist methods for extending the LSC approach to stabilized discretizations,[38] in our experience they turned out to be inefficient for the systems resulting from the RB-VMS method. Notice also that due to the coupling of $\partial_t \boldsymbol{u}_h$ with ∇q_h, the modified mass matrix appearing in the time-discretized system will have nonzero pressure rows. However, a common mixed-method iterative solver provided an approach with satisfactory efficiency.

All computations were run using the finite element library PARMOON[39] developed at WIAS Berlin. The simulations were run with 60 parallel processes on an HPE Synergy 660 Gen10 compute server with four Intel Xeon Gold 6254

TABLE 3 Mesh size and velocity/pressure space dimensions. The pair $\mathrm{P}_2^3 \times \mathrm{P}_1$ was not used on $\mathcal{T}'$ since it results in about 3,75 million degrees of freedom.

Mesh	Tetrahedra	dim($\mathrm{P_1}$)	dim($\mathrm{P_2}$)	dim($\mathrm{P_1^3 \times P_1}$)	dim($\mathrm{P_2^3 \times P_1}$)
$\mathcal{T}$	106,983	21,495	158,335	85,980	496,500
$\mathcal{T}'$	855,864	158,335	—	633,340	—

T A B L E 4 Relative computation times for a two-period simulation using the σ-model on $\mathcal{T}$ using varying numbers of parallel processes. t_{rel} is the ratio of each computation's wall time to the slowest computation.

N	t_{rel}	$15/(Nt_{\mathrm{rel}})$
15	1.000	–
21	0.815	0.876
30	0.668	0.749
45	0.560	0.595
60	0.504	0.496

CPUs, each with 18 cores clocked at 3.1 GHz. Table 4 compares relative runtimes for a two-period simulation using the σ-model on $\mathcal{T}$ with varying numbers of parallel processes, performed in sequence on the same server with minimal interference from other processes. Since a problem with constant dimension is considered for all simulations, it is expected that the efficiency of the computation does not scale ideally. In our opinion, the obtained efficiencies are satisfactory.

3.6 | Quantities of interest

This section introduces the quantities used to assess the sensitivity of the numerical results with respect to the utilized turbulence models.

3.6.1 | Pressure difference

Pressure difference across the aorta is an important quantity used to characterize the severity of the coarctation. In the numerical simulations, the pressure difference between selected planar cross-sections roughly orthogonal to the vessel centerline will be monitored. Specifically, given two cross-sections S and S', we will consider the difference between averaged pressures:

$$P_{S'} - P_S = \frac{1}{|S'|} \int_{S'} p \, d\mu_{S'} - \frac{1}{|S|} \int_{S} p \, d\mu_S.$$

3.6.2 | Maximum velocity

The value of blood velocity in the stenotic region is also a relevant indicator used in clinical practice to assess the severity of aortic stenoses. In the upcoming studies the maximum velocity $\max_X |\boldsymbol{u}|$ [m/s] through certain regions will be monitored; X may be a selected cross-section or a portion of the domain enclosed between two cross-sections.

3.6.3 | Secondary flow degree

The secondary flow degree (SFD) is a dimensionless quantity defined over a given planar cross-section as the ratio between the mean tangential (in-plane) velocity magnitude and the mean orthogonal (through-plane) velocity. Let S be a cross-section, and let $\boldsymbol{n}_S$ denote the unit normal vector on S. Then the SFD on S is defined as

$$\text{SFD}_S = \frac{\int_S |\boldsymbol{u} - (\boldsymbol{u} \cdot \boldsymbol{n}_S)\boldsymbol{n}_S| \, \mathrm{d}\mu_S}{\int_S |\boldsymbol{u} \cdot \boldsymbol{n}_S| \, \mathrm{d}\mu_S}.$$

3.6.4 | Normalized flow displacement

The normalized flow displacement (NFD) is a dimensionless number that quantifies, on a given planar cross-section, the distance of the moment of the velocity normal to the plane from the cross-section's geometric center of mass, normalized by the hydraulic radius of the cross-section. Let S denote a cross-section with geometric center of mass $\boldsymbol{x}_S$, unit normal vector $\boldsymbol{n}_S$, area A and perimeter P. Then $r_H := \frac{A}{P}$ is its hydraulic radius.[e] Now the NFD is defined as

$$\text{NFD}_S = \frac{|\boldsymbol{x}_\mathrm{n}(\boldsymbol{u}, S) - \boldsymbol{x}_S|}{r_H},$$

where

$$\boldsymbol{x}_\mathrm{n}(\boldsymbol{u}, S) := \frac{\int_S |\boldsymbol{u} \cdot \boldsymbol{n}_S| \, \boldsymbol{x} \mathrm{d}\mu_S}{\int_S |\boldsymbol{u} \cdot \boldsymbol{n}_S| \, \mathrm{d}\mu_S}.$$

3.6.5 | Wall shear stress and oscillatory shear index

The wall shear stress (WSS) quantifies the force per unit area exerted by the blood flow on the vascular endothelium, directed on the local tangent plane. Let $\boldsymbol{x} \in \partial\Omega$ be a point on the boundary, and let $\boldsymbol{n}$ be the outer unit normal at $\boldsymbol{x}$. Then the WSS at $\boldsymbol{x}$ is given by the dynamic viscosity times the normal derivative of the tangential component of the velocity, that is,

$$\tau_\mathrm{w}(t, \boldsymbol{x}) = \mu \frac{\partial}{\partial \boldsymbol{n}} (\boldsymbol{u}(t, \boldsymbol{x}) - (\boldsymbol{u}(t, \boldsymbol{x}) \cdot \boldsymbol{n})\boldsymbol{n}).$$

In our studies, the WSS τ_w was computed considering a piecewise constant normal vector on each triangular face of the boundary $\partial\Omega$ and the gradient of the velocity at the face's centroid.

The WSS is a tangential pressure exerted on the boundary, and is essentially a two-dimensional quantity. Taking a constant forward unit vector $\boldsymbol{v}$ roughly aligned with the main direction of flow near the region of interest, one can decompose the WSS τ_w into a forward (or backward) component $\tau_\mathrm{w} \cdot \boldsymbol{v}$ and a lateral component $\tau_\mathrm{w} \cdot \boldsymbol{w}$, where $\boldsymbol{w} = \boldsymbol{w}(\boldsymbol{x})$ is a unit vector orthogonal to both $\boldsymbol{v}$ and the outer normal $\boldsymbol{n}(\boldsymbol{x})$ at each point $\boldsymbol{x}$ on the reference patch. In the upcoming studies, to avoid choosing an orientation of $\boldsymbol{w}$ at each point and possibly eliminating the lateral components of boundary-touching eddies, the average of the magnitude of the lateral component

$$|\tau_\mathrm{w} \cdot \boldsymbol{w}| = |\tau_\mathrm{w} - (\tau_\mathrm{w} \cdot \boldsymbol{v})\boldsymbol{v}|$$

rather than the lateral component itself will be considered.

The oscillatory shear index[40] (OSI) is an adimensional quantity that measures the extent to which shear stress oscillates by the relative difference between the temporal mean of the shear stress vector and the mean of its magnitude, that is,
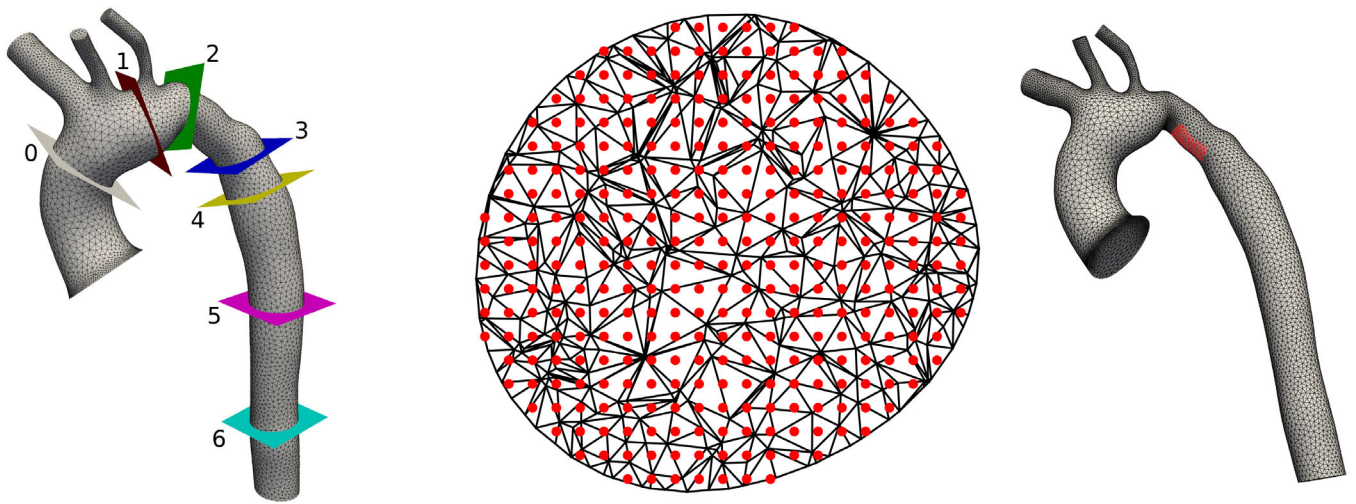
FIGURE 3   Left: positions of the planar cross-sections 0 through 6 of the aorta segment used for monitoring the quantities of interest. Middle: quadrature points on a 1 mm-resolution grid on cross-section 4. Right: reference patch for wall shear stress computation.

$$\mathrm{OSI}_I(\boldsymbol{x}) = \frac{1}{2}\left(1 - \frac{\left|\int_I \tau_{\mathrm{w}}(t, \boldsymbol{x})\mathrm{d}t\right|}{\int_I |\tau_{\mathrm{w}}(t, \boldsymbol{x})|\,\mathrm{d}t}\right)$$

for a point $\boldsymbol{x} \in \partial\Omega$ on the boundary and a time interval I. The OSI varies between 0 (shear stress always directed along the same direction) and $\frac{1}{2}$ (oscillating shear stress with zero average).

3.6.6 | Regions of interest

Average pressure, SFD, and NFD are evaluated on seven planar cross-sections S_i of the aorta segment under consideration, depicted in Figure 3 (left), with i taking the following values:

0: close to the inlet boundary, at the beginning of the aortic arch,

1: between the left common carotid and left common subclavian arteries,

2: immediately before the coarctation, where the flow narrows at the turn of the aortic arch and jet formation is expected,

3: at the end of the aortic arch,

4: at the beginning of the descending aorta, where the effects of the jet formed by inertia and the narrowing of the flow would be observable,

5: half-way between the coarctation and the outlet boundary, where the flow should begin transitioning to a simpler form, and.

6: further down the descending aorta, close to the outlet boundary, where near-laminar flow is expected.

Figure 3 (right) highlights a patch on the underside of the transition from aortic arch to descending aorta; as a "backward facing step" effect with substantial vortex formation is to be expected here, this is an interesting region on which to study the wall shear stress.

The evaluation of the other quantities of interest requires integration of the numerical solution over arbitrary planar cross-sections of the computational mesh. In our numerical studies, these integrals were approximated by defining, on each considered cross section S_i, a Cartesian grid of quadrature points at a resolution of 1 mm in each tangential direction; these points were given equal weights corresponding to $1\,\mathrm{mm}^2$ each. Additional computations with increased resolution of the grid used for numerical quadrature showed negligible influence on the QOI estimates. Table 5 lists the number of quadrature points on each plane.

We also evaluate maximum velocities on the cross-sections S_i and within the "wedges" W_j between the j-th and $(j+1)$-th cross-sections, $j = 0, \ldots, 5$.

TABLE 5 Number of points used for the calculation of cross-sectional QOIs and cross-section statistics.

Plane	0	1	2	3	4	5	6
# points	464	341	225	249	329	313	258
Area (mm^2)	462	344	225	249	328	312	257
Perimeter (mm)	76	66	53	56	64	62	57
Hydraulic radius (mm^2)	6.1	5.2	4.2	4.5	5.1	5.0	4.5

TABLE 6 Resistances (MPa s/m^3) at each outlet for the considered turbulence models and for different values of the SVR.

Turbulence model	R_{SV}	R_1	R_2	R_3	R_4
Smagorinsky, $C_{\mathrm{Sma}} = 0.01$	160	992.99	1855.9	1829.9	240.52
	115	725.77	1333.4	1282.9	172.76
	70	458.87	811.55	736.64	105.08
Smagorinsky, $C_{\mathrm{Sma}} = 0.005$	160	986.97	1858.0	1863.7	240.27
	115	719.67	1335.3	1316.6	172.48
	70	452.54	813.04	769.84	104.74
Vreman, $C_{\mathrm{Vre}} = 0.07$	160	978.57	1860.4	1902.0	240.11
	115	711.19	1337.6	1354.7	172.30
	70	443.89	814.95	807.61	104.52
σ-model, $C_\sigma = 1.35$	160	976.45	1858.7	1905.4	240.21
	115	709.05	1335.9	1358.1	172.40
	70	441.73	813.18	810.92	104.61
RB-VMS, P_1/P_1 elements	160	1004.5	1861.0	1791.6	240.44
	115	737.50	1338.8	1245.0	172.72
	70	471.02	817.77	699.56	105.15
RB-VMS, P_1/P_1 elements, fine mesh	160	984.37	1856.0	1873.5	240.30
	115	717.03	1333.3	1326.3	172.50
	70	449.85	810.87	779.39	104.75
RB-VMS, P_2/P_1 elements	160	974.81	1851.1	1880.8	240.83
	115	707.43	1328.3	1333.5	173.03
	70	440.15	805.72	786.44	105.25

4 | RESULTS

4.1 | Impact of the variation of SVR

First, an appropriate estimate for the systemic vascular resistance, see (9), should be identified and the impact of this choice studied. To this end, simulations were performed for three values $R_{\mathrm{SV}} \in \{70,115,160\}$ MPa s/m^3. The obtained results for the quantities of interest are compared below. The chosen values correspond roughly to the lower end, middle, and upper end of the adult human clinical reference range.[41]

Table 6 shows the estimated outlet resistances (Section 3.3) depending on the selected turbulence model and value of R_{SV}. The estimated values were tuned based on the outflow fractions listed in Table 2. As turbulent fluctuations produce small irregular oscillations in the outflow rates, the quality of these estimates must be evaluated over a longer time interval rather than at a single instant. We performed constant-inflow simulations with the resistances listed in Table 6; the resulting outflow errors averaged over the time interval [0.25, 0.5] satisfy

$$4\left| \int_{0.25}^{0.5} \left(\frac{Q_i(t)}{Q_i^*} - 1 \right) dt \right| < 10^{-3}$$

for each outlet $i = 1, ..., 4$.

It turned out that the impact of varying the SVR on the quantities of interest is relatively small, as shall be discussed in more detail throughout the remainder of this section. Exemplarily, results of numerical simulations performed using the Smagorinsky model with $C_{\text{Sma}} = 0.01$ and with the values of the systemic vascular resistance R_{SV} listed in Table 6 will be presented. All the results in Section 4.1 are based on a simulation time of one heartbeat, concretely in the time interval $[0.5, 1.5]$ s. As will be seen in Section 4.2, this short simulation period is justified by the negligible period-to-period variation of the results.

4.1.1 | Pressure difference

Figure 4 shows the pressure difference between each cross-section and cross-section 0 averaged over one pulse period (left) as well as the difference between cross-sections 4 and 2 (right), that is, between the aortic arch just past the left common subclavian artery and the upper descending aorta, straddling the coarctation.

The time-averaged pressure difference varies by less than 2 Pa between the three values of R_{SV}. The largest variations in the difference between cross-sections 4 and 2 over time occur just before systole and at the end of the decelerating phase (around 1 and 1.25 s), with maximum differences around 62 Pa and a mean of less than 4 Pa. The pressure differences between other pairs of cross-sections behave comparably.

4.1.2 | Maximum velocity

Figure 5 compares the maximum velocities through the wedge between cross-sections 2 and 3 (left) and through cross-section 6 (right) over time. The results are again very close, though minor quantitative differences appear particularly when the flow is less rapid overall.

4.1.3 | Secondary flow degree

The secondary flow degree across each cross-section averaged over one pulse period (left) as well as across cross-section 6 over time (right), that is, the last cross-section before the lower end of the computational domain, are depicted in
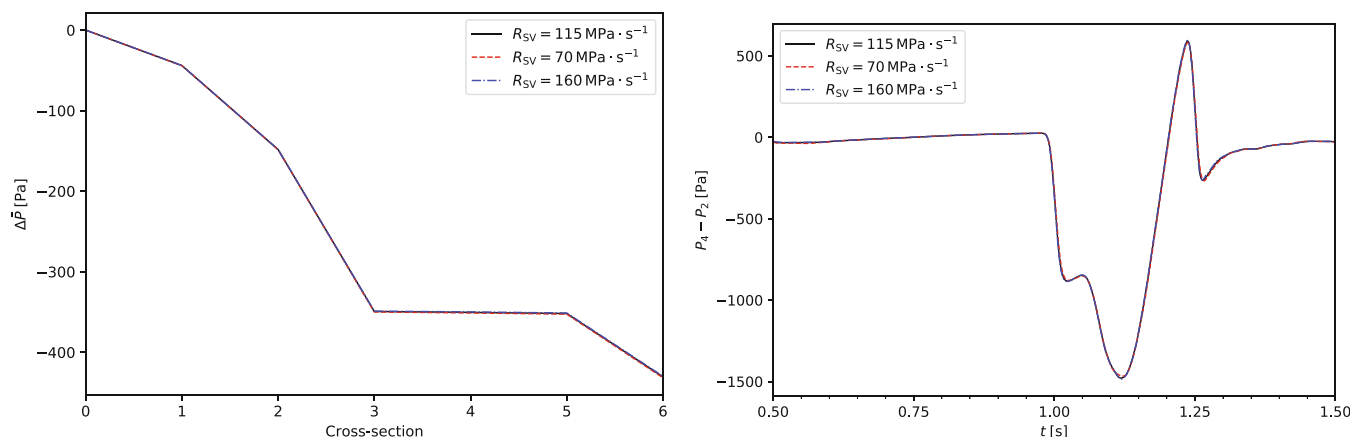
FIGURE 4 Impact of the variation of SVR. Left: time-averaged pressure difference on each cross-section. Right: pressure difference between cross-sections 4 and 2 over time. Simulations with Smagorinsky model, $C_{\text{Sma}} = 0.01$, varying R_{SV}.
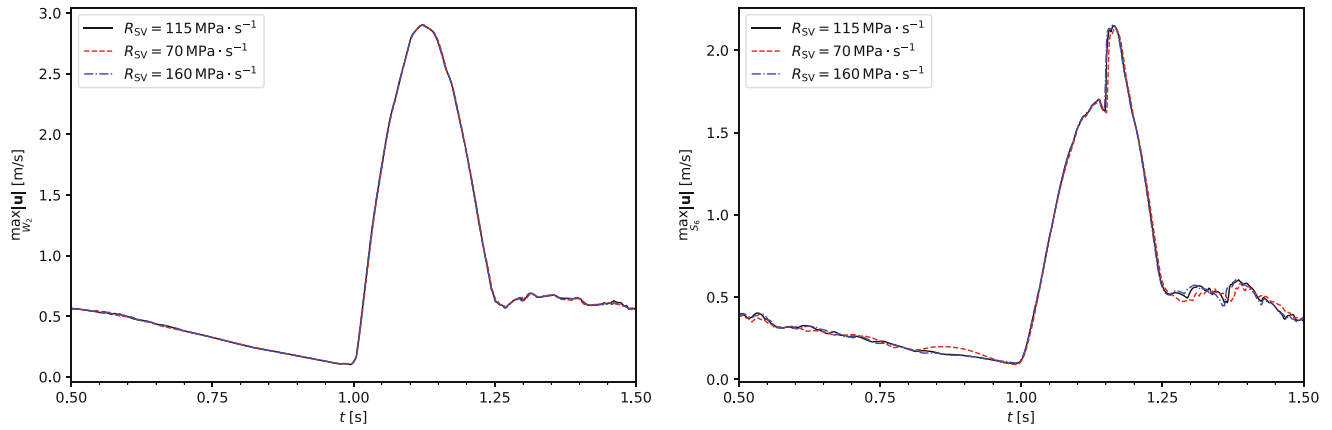
FIGURE 5 Impact of the variation of SVR. Left: maximum velocity through the wedge between cross-sections 2 and 3 over time. Right: maximum velocity through cross-section 6 over time. Simulations with Smagorinsky model, $C_{Sma} = 0.01$, varying R_{SV}.
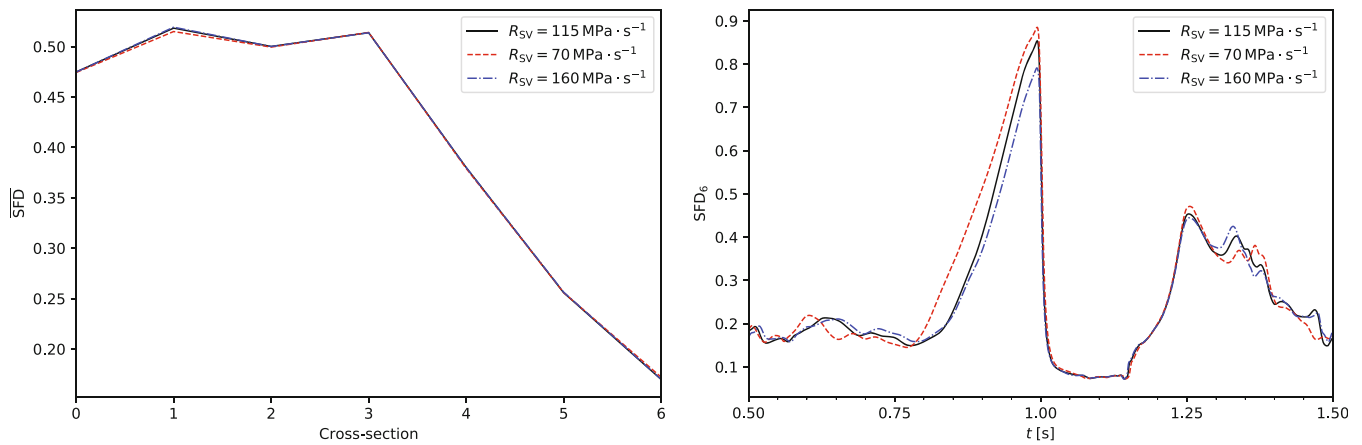

FIGURE 6 Impact of the variation of SVR. Left: time-averaged secondary flow degree per cross-section. Right: secondary flow degree across cross-section 6 over time. Simulations with Smagorinsky model, $C_{Sma} = 0.01$, varying R_{SV}.

Figure 6. This cross-section was chosen because it exhibits the most visible differences. Note that the time-averaged SFD was computed not by time-averaging the instant SFD but by the ratio of cumulative tangential flow to cumulative normal flow:

$$\overline{\text{SFD}}_S = \frac{\int_{0.5}^{1.5} \int_S |\boldsymbol{u} - (\boldsymbol{u} \cdot \boldsymbol{n})\boldsymbol{n}| \, d\mu_S dt}{\int_{0.5}^{1.5} \int_S |\boldsymbol{u} \cdot \boldsymbol{n}| \, d\mu_S dt}.$$

As for the pressure difference, the values of time-averaged SFD vary negligibly for different choices of R_{SV}. The largest absolute difference is found at cross-section 1 (just before the brachiocephalic artery), where the values range from 0.50439 to 0.50743.

Larger differences are visible plotting the SFD across cross-section 6 over time. However, the qualitative behavior is largely unaltered, lower resistances corresponding roughly to a higher peak just before systole and shifts in time and amplitude of the irregular oscillation during diastole.

4.1.4 | Normalized flow displacement

Figure 7 shows the normalized flow displacement across each cross-section averaged over one pulse period (left) as well as across cross-section 3 over time (right), that is, the first cross-section past the coarctation, chosen due to its position near the center of a prominent jet. Note that the time-averaged NFD has been weighted by the normal flow rate:

$$\overline{\mathrm{NFD}}_S = \frac{\int_{0.5}^{1.5} \int_S |\boldsymbol{u} \cdot \boldsymbol{n}| \, \mathrm{d}\mu_S \mathrm{NFD}_S(t) \mathrm{d}t}{\int_{0.5}^{1.5} \int_S |\boldsymbol{u} \cdot \boldsymbol{n}| \, \mathrm{d}\mu_S \mathrm{d}t}.$$

Also in this case, the time-averaged quantity shows only negligible differences: the largest absolute differences are at cross-section 6, where the NFD ranges from 0.05704 to 0.05885. As for the SFD, the effect of the different SVR on the temporal variation amounts to slight shifts of the peaks and valleys in time and amplitude.

4.1.5 | Wall shear stress

Figure 8 presents the magnitude of the wall shear stress and of its "forward" component, that is, the component in the main direction of flow, averaged over the reference patch depicted in Figure 3 (right). Also in this case, only minor differences are visible.

Finally, Table 7 provides information on the time-averaged WSS magnitude and the OSI values over one pulse period. Both WSS and OSI increase for increasing R_{SV}. However, in the considered SVR range, the differences are less than 1%.

4.2 | Impact of turbulence model selection

This section starts by providing an overall comparison of the flow field obtained with some of the considered turbulence models. Next, the results with respect to the considered quantities of interest will be presented in detail. The time-averaged quantities were computed for all turbulence models for one pulse period, concretely in the time interval $[0.5, 1.5]$ s. In addition, for selected models, long-term computations were performed over a longer time interval of 31 periods, in order to investigate the differences from period to period. In this case, results are shown in terms of long time-averages over the interval $[1, 31]$ s (30 periods), discarding the first time interval used for a smooth start, as well as considering an averaged period, in which the results at each time $t \in [0, 1]$ s are computed by averaging the results over
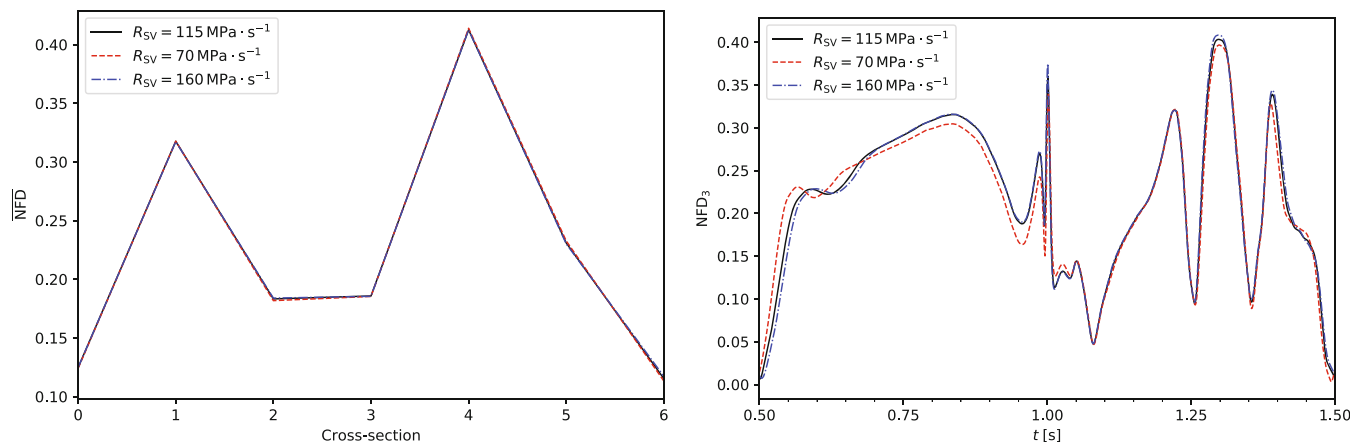

FIGURE 7 Impact of the variation of SVR. Left: time-averaged normalized flow displacement per cross-section. Right: normalized flow displacement across cross-section 3 over time. Simulations with Smagorinsky model, $C_{Sma} = 0.01$, varying R_{SV}.
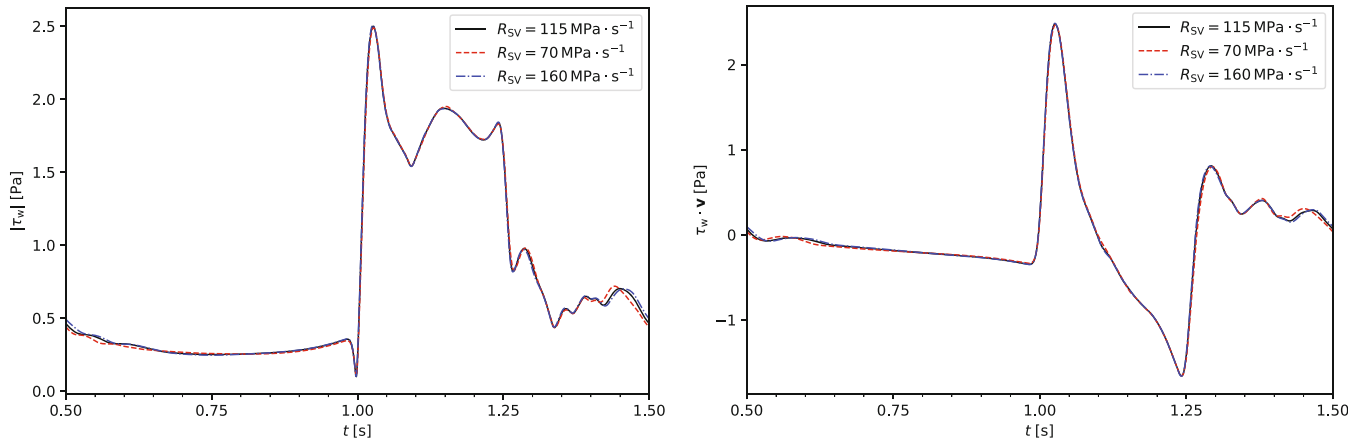
FIGURE 8 Impact of the variation of SVR. Left: average wall shear stress magnitude over reference patch (see Figure 3, right). Right: average forward wall shear stress (shear stress along the main flow direction) over reference patch. Simulations with Smagorinsky model, $C_{\mathrm{Sma}} = 0.01$, varying R_{SV}.

TABLE 7 Impact of the variation of SVR. Time-averaged WSS magnitude and OSI over reference patch. Simulation with the Smagorinsky model, $C_{\mathrm{Sma}} = 0.01$.

R_{SV} (MPa $\cdot$ s/m^3)	$\lvert \tau_{\mathrm{w}} \rvert$ (Pa)	OSI
70	0.76756	0.45781
115	0.77128	0.45779
160	0.77321	0.45792

the 30 periods at the corresponding time steps $t + i$, $i = 1, \ldots, 30$. Additionally, period-wise minima and maxima are plotted as dotted lines matching the color of the corresponding mean; in the case of time-averaged quantities of interest, these are the minima and maxima of single-period averages. In light of the relatively small influence of the systemic vascular resistance, the simulations presented in this section were all performed using $R_{\mathrm{SV}} = 115$ MPa s/m^3.

4.2.1 | Flow field

For the sake of brevity, this section focuses on the RB-VMS model used in combination with P_1/P_1 elements, since this is the only approach that uses first-order elements for the velocity.

Figures 9 and 10 present the flow fields computed with the RB-VMS model (P_1/P_1) at one time instant at peak flow and another time instant in the decreasing phase, where in the latter figure also the corresponding picture for the σ-model is shown. It can be observed that the flow fields for the RB-VMS model (P_1/P_1) are rather smooth, in particular on the coarse mesh. Using a low-order velocity space introduces therefore a comparatively large amount of numerical diffusion.

This observation is confirmed by the quantitative comparisons in the top row of Figure 11, showing that the velocity field computed with the RB-VMS model using equal-order linear elements decays more quickly with decreasing inflow, especially on the coarse mesh. The simulations with second order velocity retain finer features, resulting in slower dissipation of energy carried by small eddies.

The bottom row of Figure 11 shows, as a measure of resolved turbulent variation, the long-time simulations' standard deviations of the kinetic energy

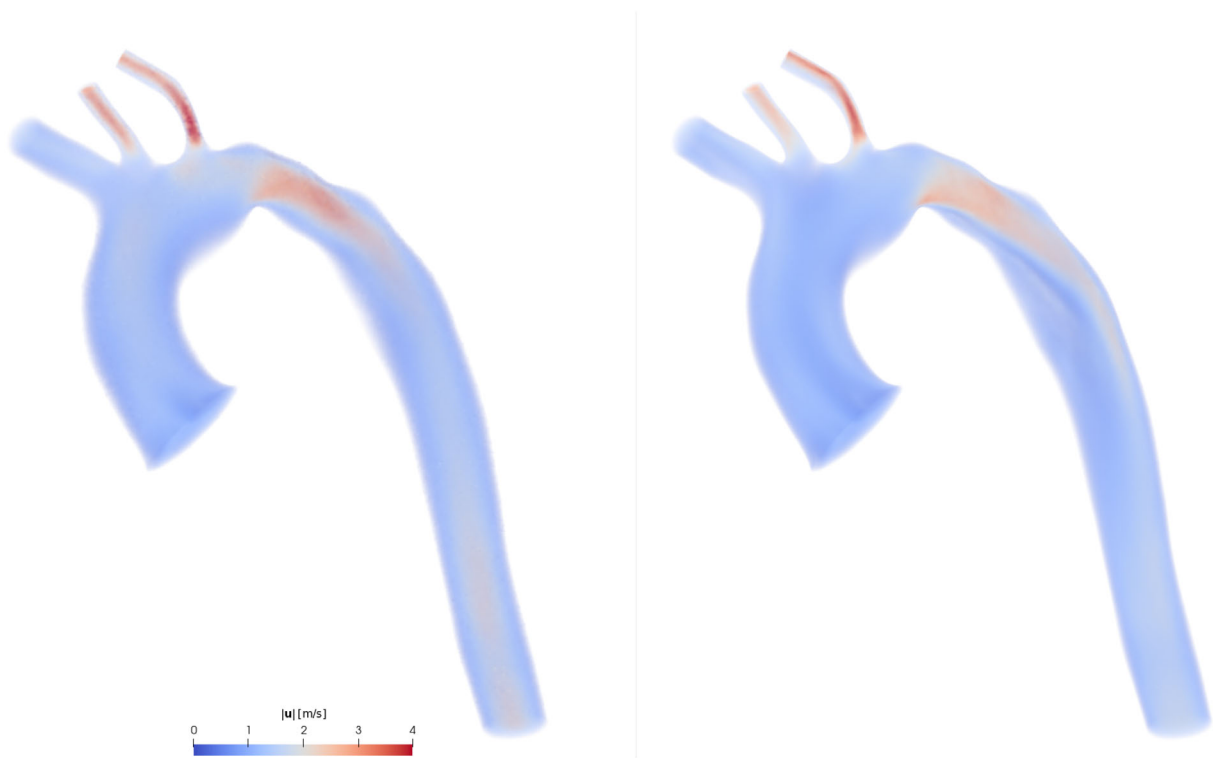$$k' = \frac{\rho}{2} \int_{\Omega} \sigma^2(\boldsymbol{u}) \mathrm{d}\boldsymbol{x},$$

FIGURE 9 Magnitude of the velocity field (volume plot) $t = 1.125$s (peak inflow) for the RB-VMS model, P_1/P_1 elements. Left: Solution on the coarse mesh. Right: Solution on the fine mesh.
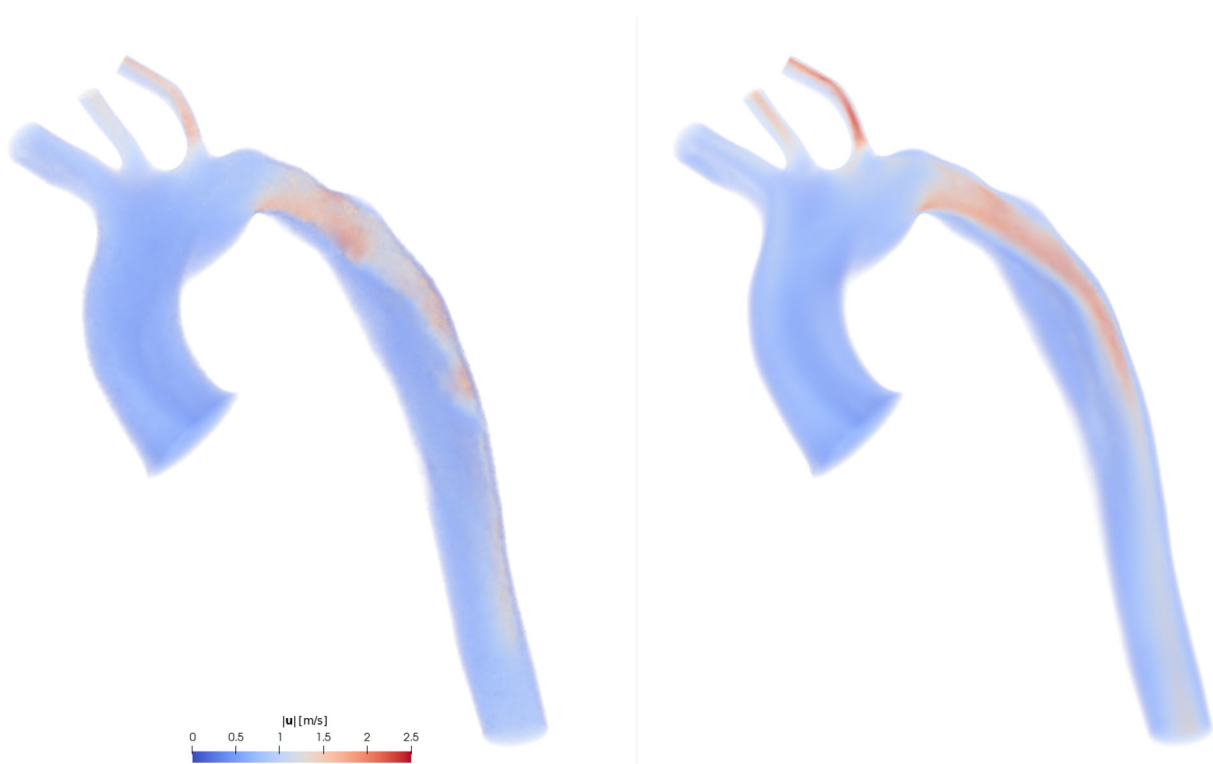

FIGURE 10 Magnitude of the velocity field (volume plot) at $t = 1.2$s (decelerating phase). Left: σ-model, $C_\sigma = 1.35$. Right: RB-VMS, P_1/P_1 elements, fine mesh.
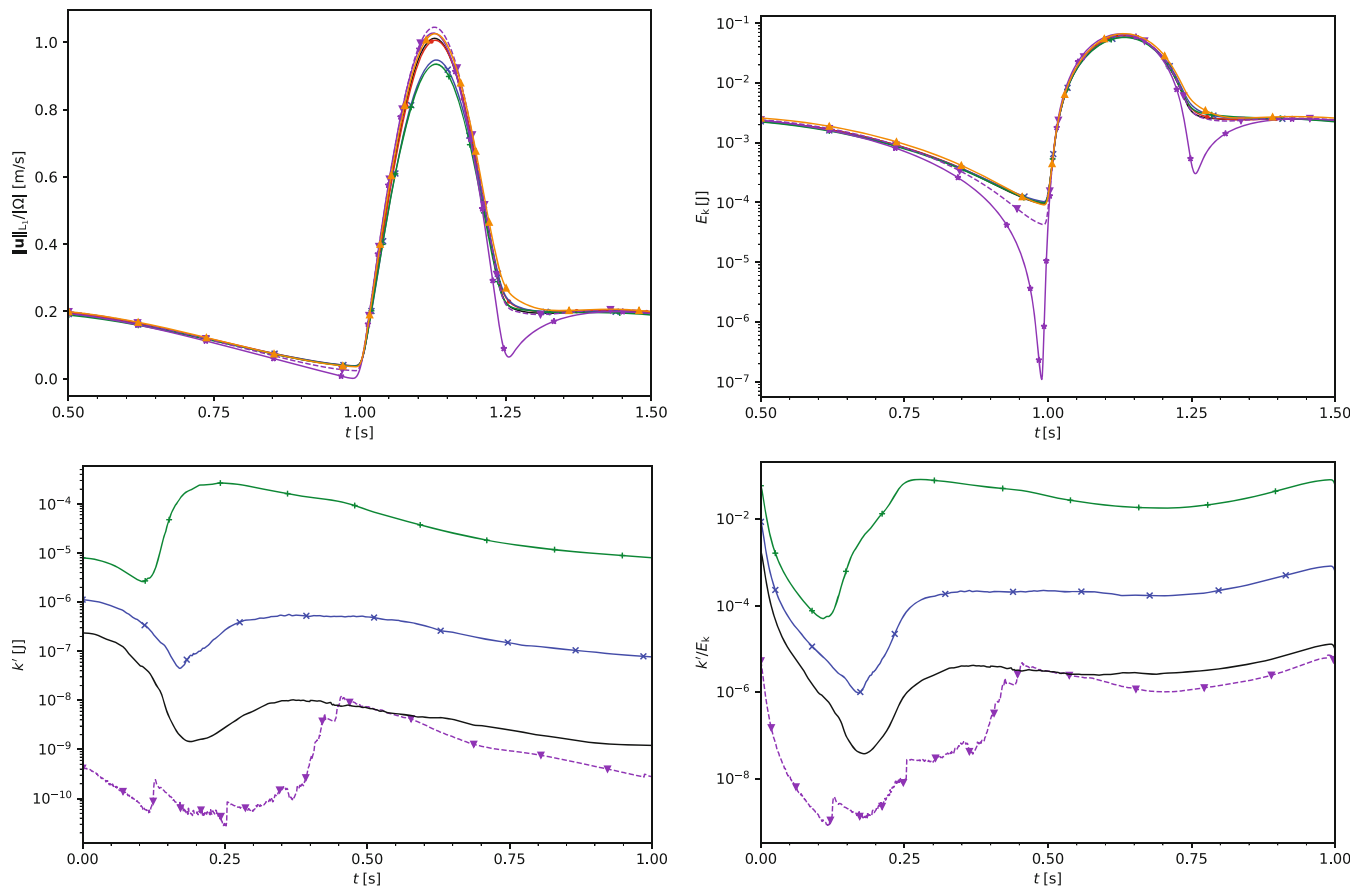
FIGURE 11 Upper left: spatially averaged velocity magnitude over time. Upper right: kinetic energy over time. Lower left: Long-time velocity deviation. Lower right: Ratio of long-time velocity deviation to period-averaged kinetic energy. The legend is given in Figure 12.

FIGURE 12 Common legend for the figures describing the comparison among turbulence models.

with $\sigma^2(\boldsymbol{u})$ being the variance of $\boldsymbol{u}$, and its ratio to the total kinetic energy over time. This differs from steady-inflow notions of turbulence kinetic energy in that the deviation is computed at each point $\boldsymbol{x} \in \Omega$ and each time instant $t \in [0,1]$ s by taking the deviation over the corresponding time instants $t+i$, $i=1,...,30$, of each simulated period following the warmup. Here the RB-VMS results with piecewise linear velocities clearly resolve less variation than those computed with other models, particularly during systole, whereas the σ-model clearly exceeds the others.

4.2.2 | Pressure difference

Figure 12 shows the legend convention used for the detailed comparison of turbulence models below. Figures 13 and 14 present the results for the cross-sectional pressures.
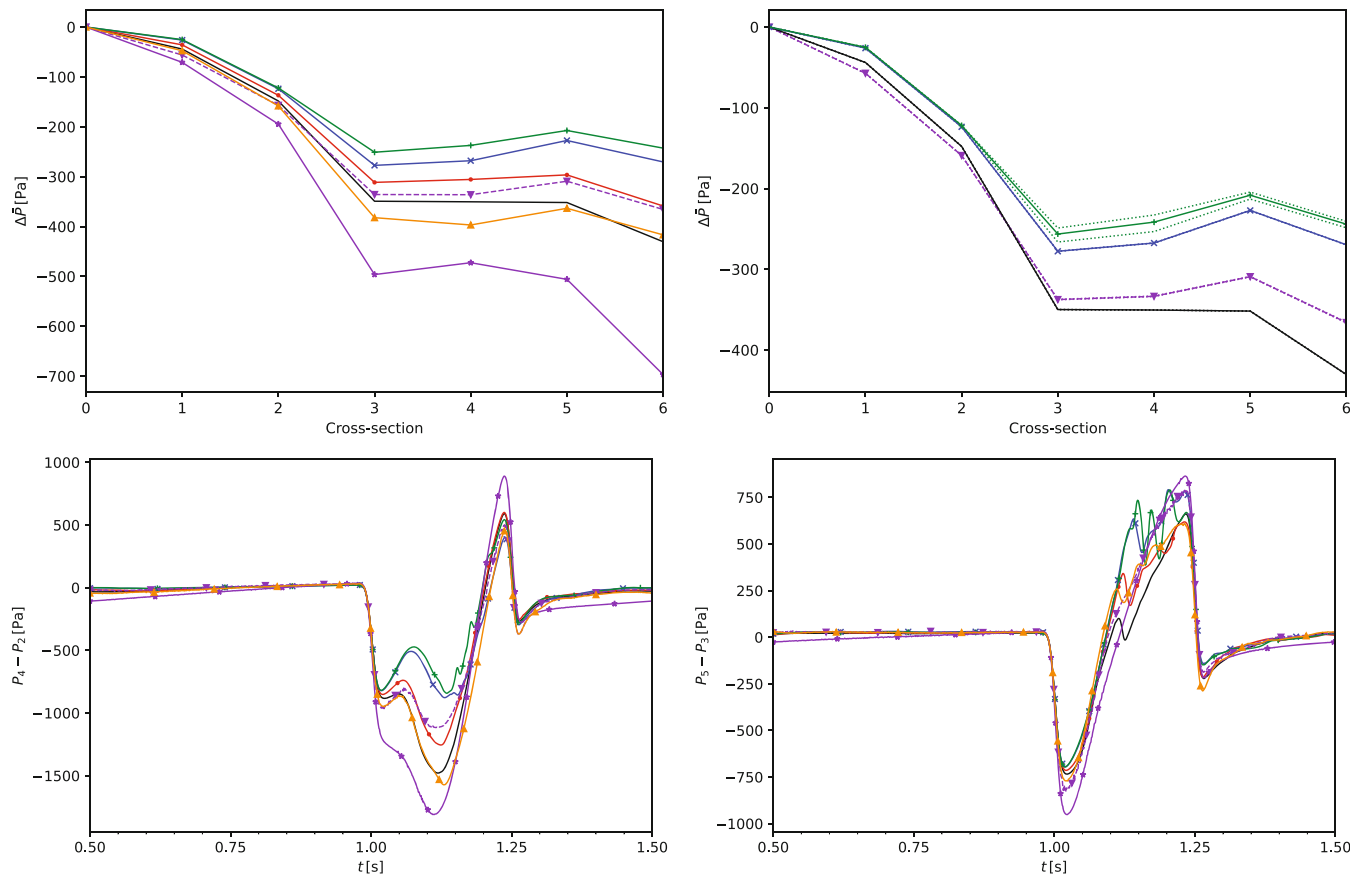
FIGURE 13 Upper left: time-averaged pressure difference per cross-section. Upper right: long time-averaged pressure difference per cross-section. Dotted lines indicate minimum and maximum of single-period averages. Lower left: pressure difference between cross-sections 4 and 2 over time. Lower right: pressure difference between cross-sections 5 and 3 over time. The legend is given in Figure 12.

The plots in the upper row of Figure 13 depict the difference with respect to the first cross section. Mean pressures are averaged over a single period (upper-left) and over the longer interval of 30 periods (upper-right). The lower pictures show the pressure difference between two selected pairs of cross-sections over one pulse period.

Figure 14 instead shows, in the upper row, the instantaneous pressure differences at peak flow, for one period (left) and averaged over 30 periods (top right).

Although the qualitative behavior is similar, the models differ widely in scale. The RB-VMS model with P_1/P_1 elements on the coarse mesh in particular shows a pronounced overestimation of pressure differences compared to the other models, which is likely an artifact of the excessive numerical dissipation discussed above. Refining the mesh results in values closer to the other models. The average pressure differences computed with the σ-model and the Vreman model are very similar for all cross-sections; the results computed using the Smagorinsky model with $C_{Sma} = 0.005$ is closer to these than those computed using $C_{Sma} = 0.01$. The latter results, in turn, are close to those obtained with the RB-VMS model with P_2/P_1 elements.

Discarding the RB-VMS model with P_1/P_1 elements on the coarse mesh, the largest time-averaged pressure difference is still about twice the smallest. For instance, the difference between cross-sections 4 and 2 ranges from 115.2 Pa (σ-model, $C_\sigma = 1.35$) to 238.7 Pa (RB-VMS model with P_2/P_1 elements).

Whereas the average pressure increases slightly from cross-section 3 to cross-section 5 in most models, by up to 49.9 Pa for the Vreman model with $C_{Vre} = 0.07$, the Smagorinsky model with $C_{Sma} = 0.01$ exhibits a decrease by 2.6 Pa. The RB-VMS model with P_1/P_1 elements on the coarse mesh is the only other model not to show an increase here.

The pressures at peak flow behave similarly. Peak pressure generally occurs during acceleration, slightly before peak flow.
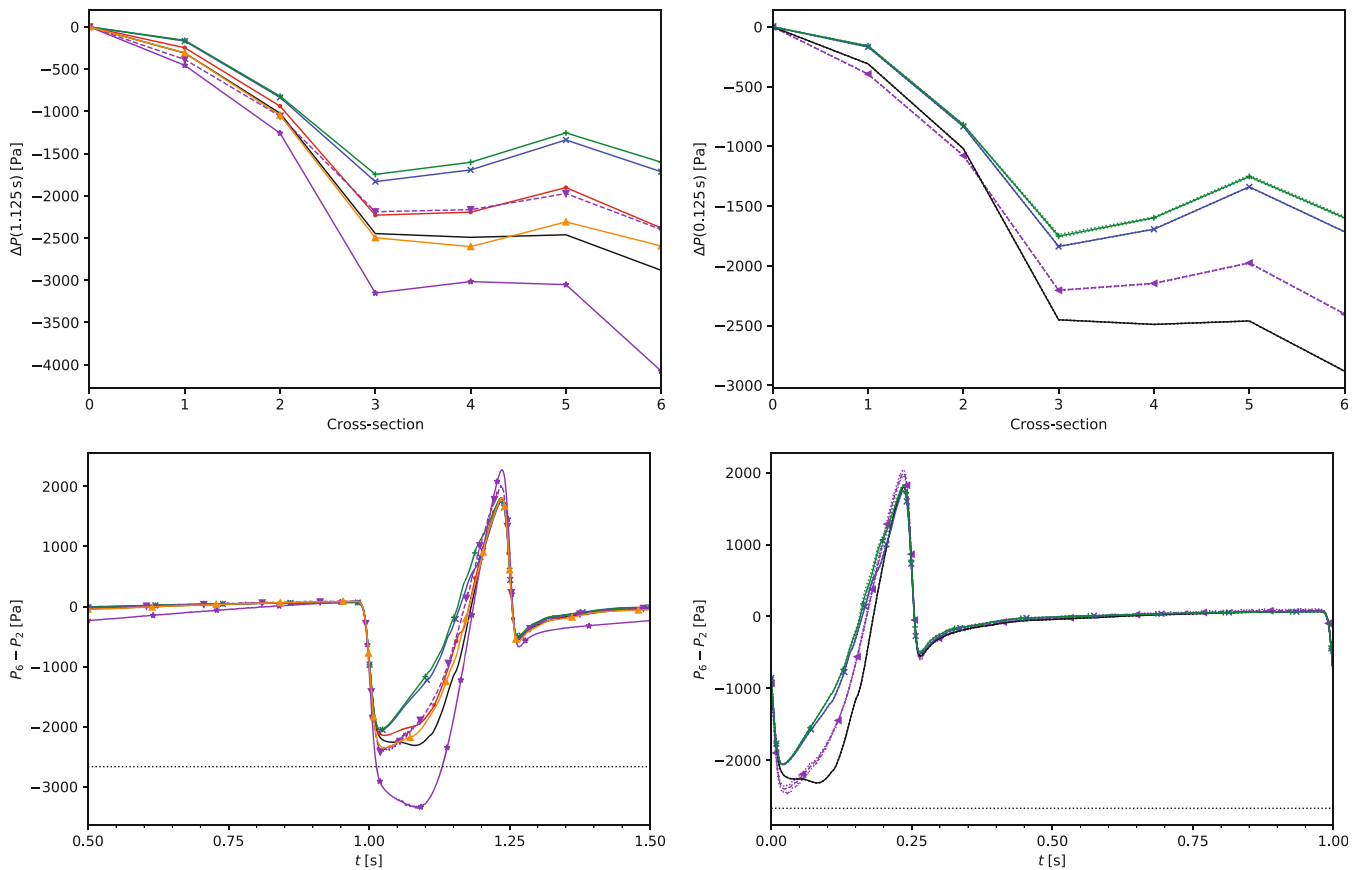
FIGURE 14 Upper left: pressure difference per cross-section at peak flow. Upper right: pressure difference per cross-section at peak flow averaged over all simulation periods. Dotted lines indicate period-wise minimum and maximum. Lower left: pressure difference between cross-sections 6 and 2 over time. Lower right: pressure difference between cross-sections 6 and 2 over time over a heartbeat, averaging the results for the corresponding time instant over the simulated beats. Dotted lines indicate period-wise minimum and maximum. The 20 mmHg threshold, which is considered an indication of severe coarctation, is marked by a dotted line. The legend is given in Figure 12.

Looking at the pressure's behavior over time gives some insight into these differences. Every model exhibits an inversion of the pressure difference between consecutive cross-sections as the flow decelerates towards diastole, as one would expect. However, as a prominent jet forms at the narrowed exit of the aortic arch and begins to shed vortices beneath it, an inverted pressure gradient emerges from the jet's deceleration as it dissipates into the wider descending aorta, and the pressure waves associated with the shed vortices manifest as oscillations in the pressure plots in Figure 13. These effects emerge earlier and more clearly in the results given by less diffusive models, particularly the σ-model. In other models, increased numerical diffusion results in a much cleaner jet that remains coherent further down the descending aorta (compare Figures 9 and 10), resulting in the larger pressure difference between cross-sections 2 and 4 (compare Figure 13, lower left).

In Figure 14 (bottom row), an additional dotted line shows the pressure difference of 20 mmHg. Peak systolic pressure exceeding this value is indicated in recent guidelines as a marker of a severe coarctation.[3,4] One can see that only the RB-VMS model with P_1/P_1 on the coarse mesh exceeds the 20 mmHg threshold. While the finer models vary in the shape and timing of the pressure peak during acceleration, this peak remains in all cases slightly below the critical threshold.

The long-term averages show very little distinction from period to period in all simulations except those using the σ-model. Here, one can observe that moderate period-wise differences increase after the coarctation, as the eddying around the jet is not identical each time. The overall effect of this behavior on the pressure is smaller further down the aorta, where the downward flow begins to relaminarize somewhat as the smallest eddies dissipate.

4.2.3 | Maximum velocity

Figure 15 displays the maximum velocity magnitude over the wedge between cross-sections 2 and 3 (top), straddling the coarctation, and across cross-section 6 (bottom), further down the descending aorta.

The maximum stenotic velocity (the peak in Figure 15, top row) shows a clustering of most models around 3.1 m/s. The RB-VMS models on the coarse mesh notably exceed this value, while the Smagorinsky model with $C_{Sma} = 0.01$ yields a slightly lower peak velocity (2.9 m/s). In image-based clinical assessment, this range of values might indicate the presence of a mild stenosis, but it is well below the critical value of 5 m/s considered as a marker of a severe condition.

The behavior of the velocity in the descending aorta (Figure 15, bottom), while less clinically relevant, is helpful in distinguishing the models' behaviors. The eddy viscosity models each match the jet's development by showing a distinct dip followed by a secondary peak, but the height and timing vary considerably. The RB-VMS model with P_1/P_1 elements——notably on both meshes—behaves much more smoothly and indistinctly. The decaying vortices shed by the jet above are also much less visible in these models' plots during diastole.

Only the σ model shows minor variability from period to period, particularly during diastole.
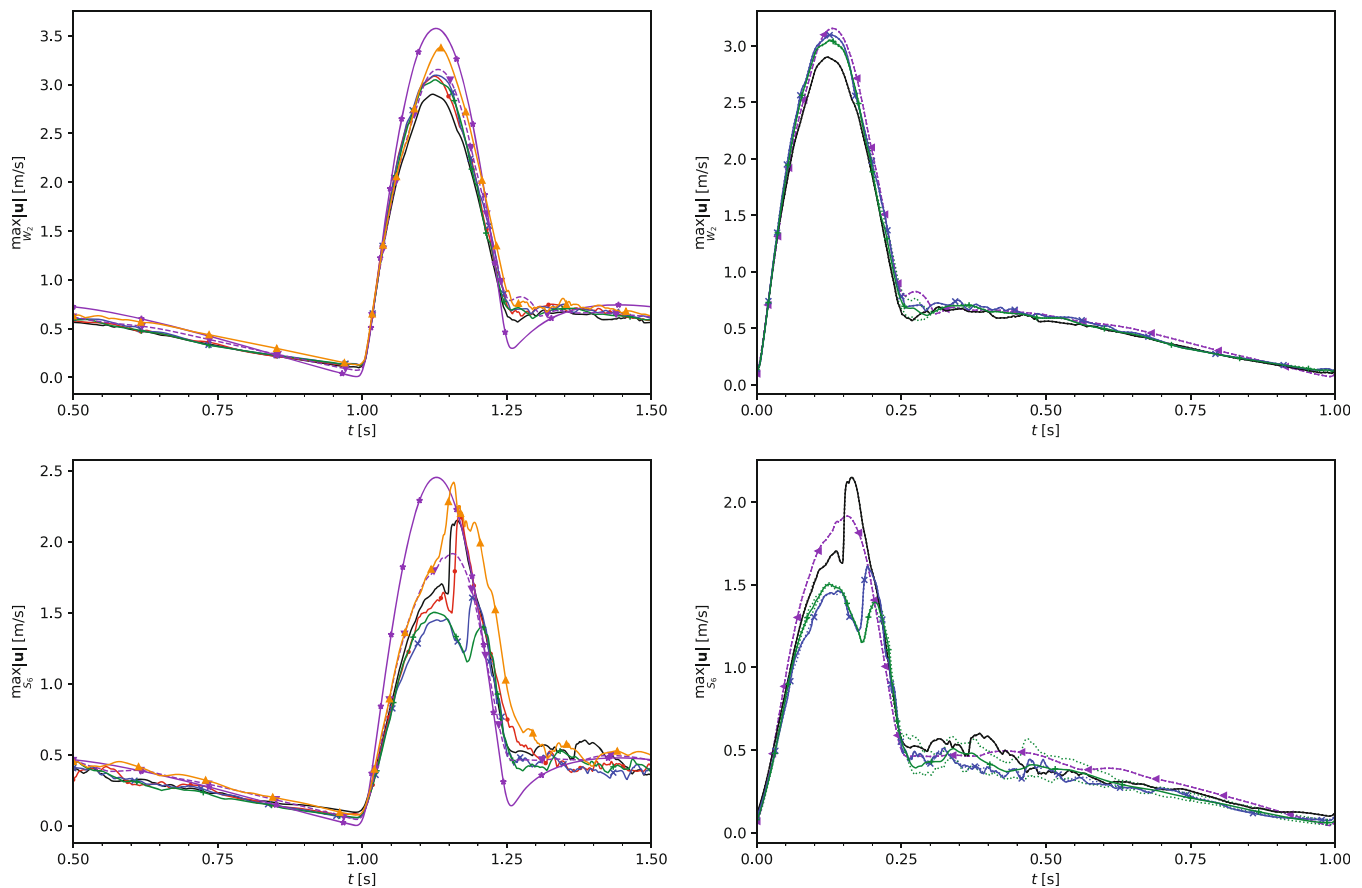

FIGURE 15 Upper left: maximum velocity through the wedge between cross-sections 2 and 3 over time. Upper right: maximum velocity through the wedge between cross-sections 2 and 3 over time over a heartbeat, averaging the results for the corresponding time instant over the simulated beats. Dotted lines indicate period-wise minimum and maximum. Lower left: maximum velocity through cross-section 6 over time. Lower right: maximum velocity through cross-section 6 over time over a heartbeat, averaging the results for the corresponding time instant over the simulated beats. Dotted lines indicate period-wise minimum and maximum. The legend is given in Figure 12.

4.2.4 | Secondary flow degree

The secondary flow degree averaged over time is shown in Figure 16 (top). Excluding the RB-VMS model with P_1/P_1 elements on the coarse grid, which delivers numerical results which are clearly different from all other models, the time-averages are clustered rather closely together. The largest difference between models is 0.127 (on cross-section 5) when the refined P_1/P_1 model is included; the largest difference between the P_2/P_1 models is 0.071 (on cross-section 3).

The plots of the SFD across two cross-sections over time (Figure 16, bottom) show a more irregular behavior. However, the curves exhibit peaks and valleys at roughly the same times for most models: SFD increases as the velocity field decays away from forward flow towards the end of diastole, then decreases rapidly as the inflow begins to accelerate (from $t = 1$–1.05 s). The vortex shedding in the descending aorta (see also the pronounced jet visible in Figure 10) increases well before peak inflow time ($t = 1.125$ s), and the SFD peaks again just before the secondary inflow increase visible in Figure 2.

Apart from small peaks around the inflow minima, the SFD predicted with the P_1/P_1 RB-VMS model on the coarse grid remains almost constant, close to its minimum, indicating effectively laminar flow not precisely normal to the cross-section. In the long term simulation the σ-model is the only one to show a large variation in the SFD from period to period. Here, the differences in position and dissipation of the vortices formed below the jet at the exit of the aortic arch lead to substantial SFD variation in the upper descending aorta.

These first figures show that the results obtained with the P_1/P_1 RB-VMS model on the coarse grid are very inaccurate for the quantities of interest discussed so far, while using a second order velocity in the RB-VMS model or refining
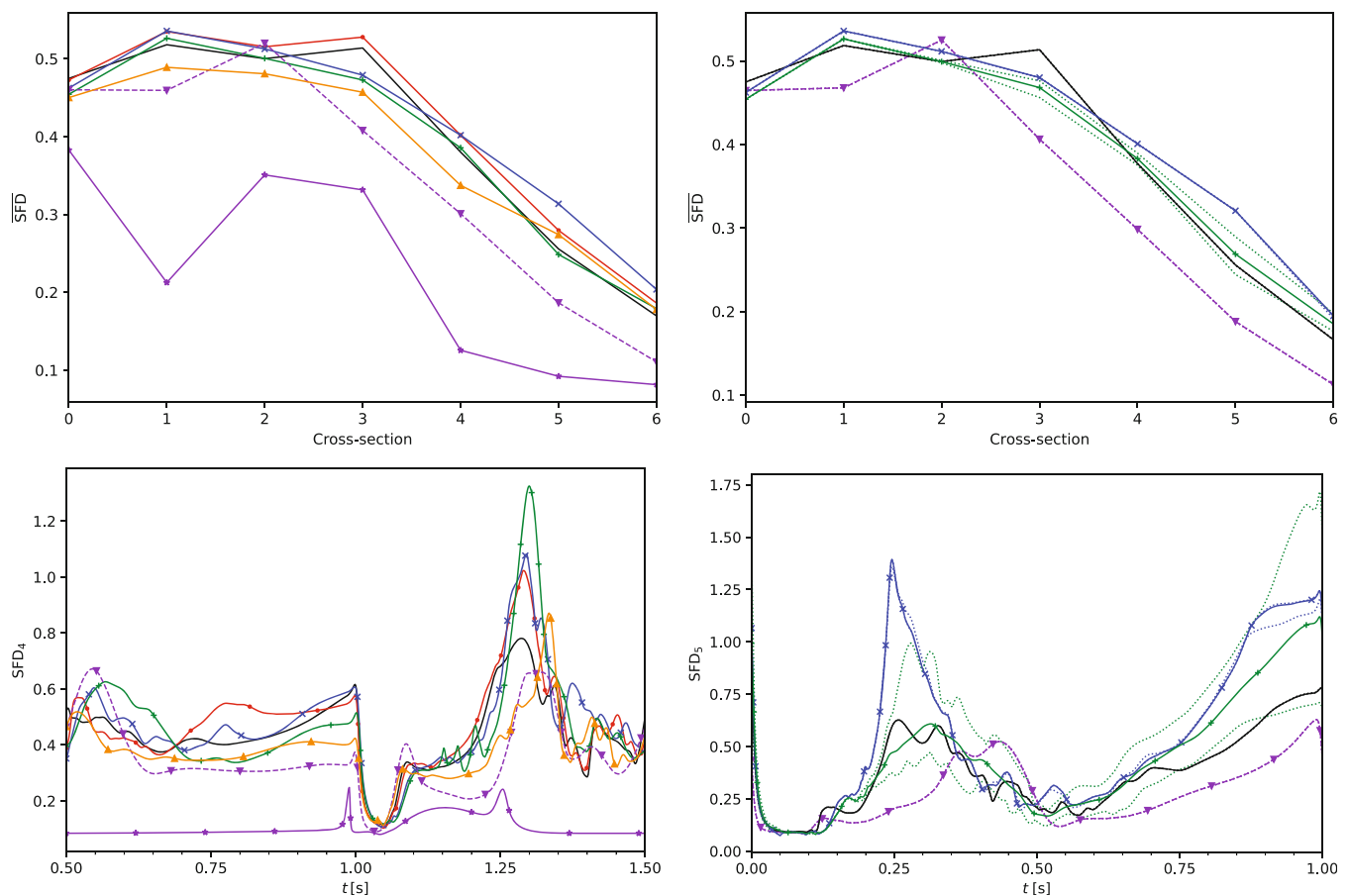

FIGURE 16 Upper left: time-averaged secondary flow degree per cross-section. Upper right: long time-averaged secondary flow degree per cross-section. Dotted lines indicate the minimum and maximum of single-period averages. Lower left: secondary flow degree across cross-section 4 over time. Lower right: secondary flow degree across cross-section 5 over time during a heartbeat, averaging the results for the corresponding time instant over the simulated beats. Dotted lines indicate period-wise minimum and maximum. The legend is given in Figure 12.

the mesh gives results that are much more similar to the other models. The results of this model will no longer be discussed in detail below, although the corresponding results will still be displayed in the figures.

4.2.5 | Normalized flow displacement

Results for the normalized flow displacement are presented in Figure 17. It is noteworthy that the results for the RB-VMS model with P_1/P_1 elements on the finer grid differ considerably from the others. However, using second-order velocity on the coarse grid leads to qualitatively the same behavior as predicted by the other methods.

All curves show substantial differences on at least one cross-section. The results obtained with the Vreman model and the σ-model differ significantly only on cross-section 5. This cross-section is also the only one on which the two Smagorinsky models do not predict a similar average NFD.

Looking at the NFD behavior over time (Figure 17, bottom), one sees a more irregular dynamics than those of the pressure differences or of the SFD, especially during the phases with lower velocity. This observation is not surprising, as a largely undirected flow dominated by decaying fluctuations should be expected not to have a strongly defined center. Nevertheless, during systole, the eddy viscosity models lead to more similar results. It is perhaps notable that the Vreman and σ-models, which are conceptually the most concerned with avoiding unnecessary artificial dissipation, exhibit oscillations as the flow decelerates.

As with pressure differences and the SFD, the σ-model shows by far the most variation from period to period in the long time simulation. This effect is largely due to the fact that, as the consistent forward flow disappears during the
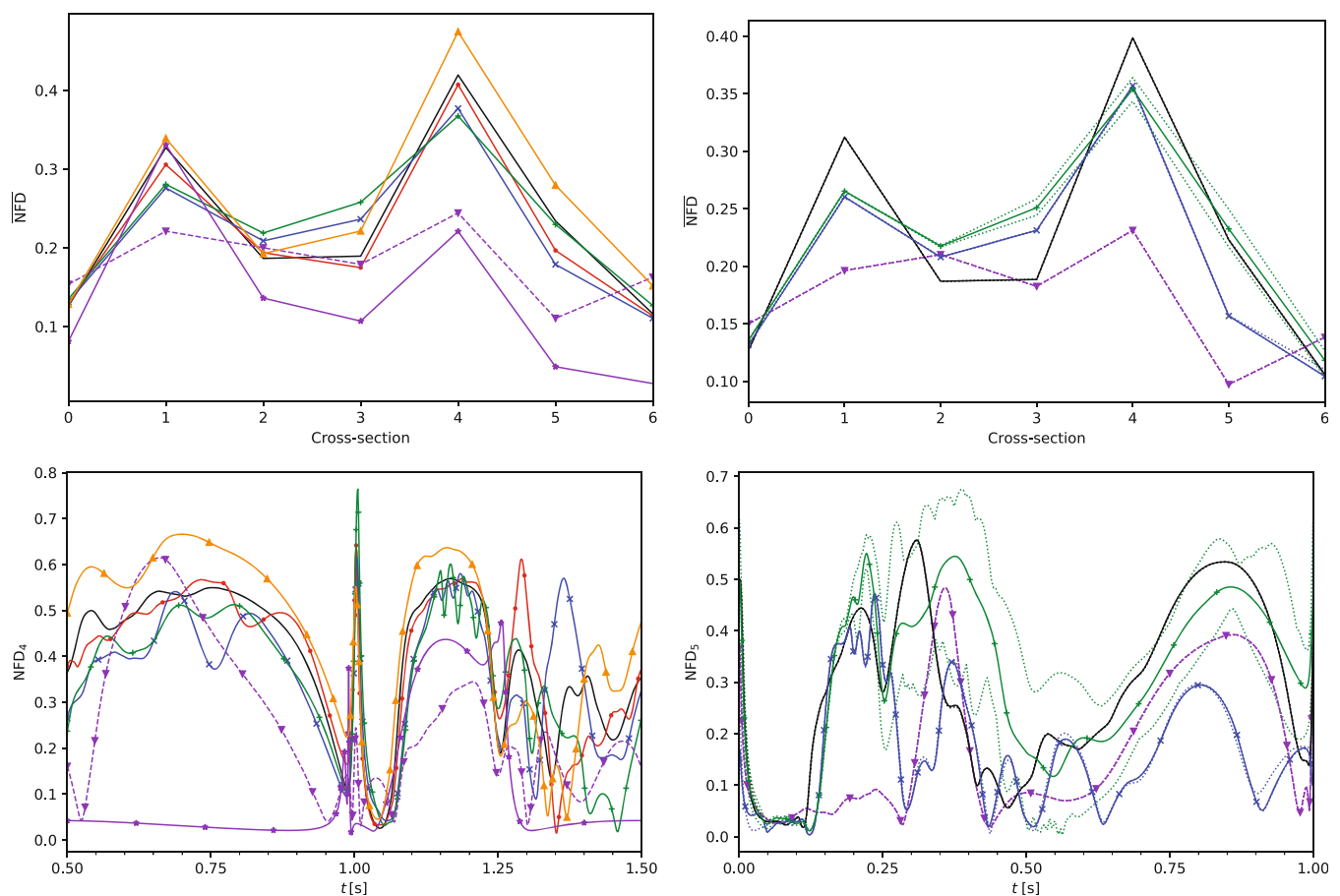

FIGURE 17 Upper left: time-averaged normalized flow displacement per cross-section. Upper right: long time-averaged normalized flow displacement per cross-section. Dotted lines indicate minimum and maximum of single-period averages. Lower left: normalized flow displacement across cross-section 4 over time. Lower right: Normalized flow displacement across cross-section 5 over time during a heartbeat, averaging the results for the corresponding time instant over the simulated beats. Dotted lines indicate period-wise minimum and maximum. The legend is given in Figure 12.

decelerating phase, the normal components of slowly dissipating eddies begin to dominate. As previously observed, the period-wise variation of these eddies is much less prominent in the other models.

Figure 18 shows the normal component of the velocity across cross-section 4 at time instant $t = 1.107$ s computed using the three RB-VMS models and using the σ-model. In this case, one can observe large differences of the NFD across these models. Investigating the slices suggests some weakness in the NFD's ability to characterize ring-like flow structures. In fact, the RB-VMS model with P_1/P_1 elements on the refined mesh (upper right) has the smallest NFD of these four examples, despite the clearly visible concentration of the forward flow near the cross-section's boundaries.
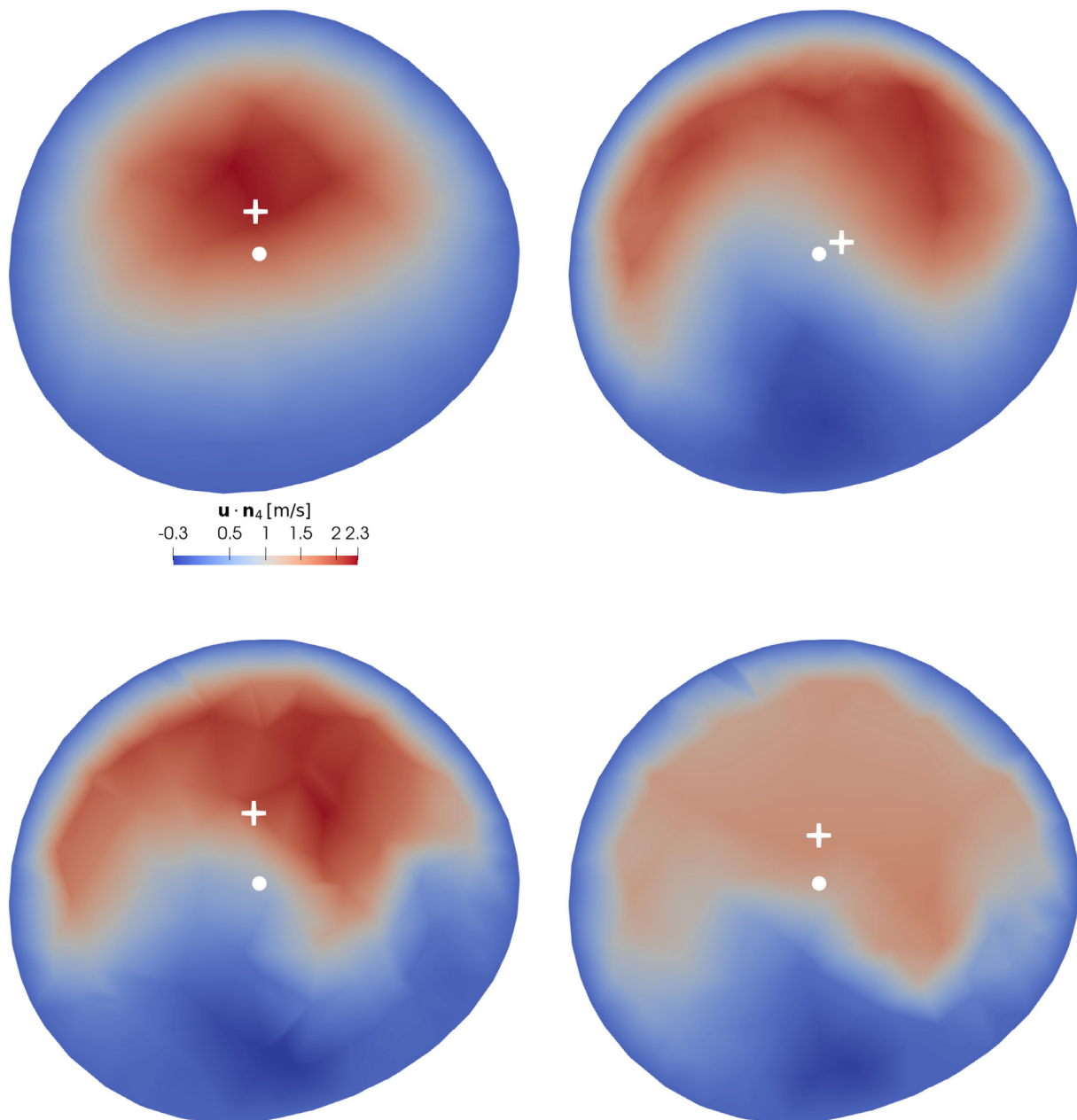
FIGURE 18 Normal velocity across cross-section 4 at time $t = 1.107$ s (late accelerating phase). The geometric center of mass of the cross section is marked with a circle, while the normal flow moment is marked with a cross. Upper left: RB-VMS model with P_1/P_1 elements. Upper right: RB-VMS model with P_1/P_1 elements, fine mesh. Lower left: RB-VMS model with P_2/P_1 elements. Lower right: σ-model, $C_\sigma = 1.35$.

4.2.6 | Wall shear stress

Figure 19 presents the space-averaged magnitude (upper left), the forward component (upper right), and the lateral magnitude (lower right) of the wall shear stress over the reference patch shown in Figure 3 (right), as well as the WSS magnitude averaged over the entirety of Γ_{wall} (lower left). Table 8 lists the time-averaged WSS magnitude and the OSI over the reference patch, as in Section 4.1.5. Here, the models differ widely in scale. Unsurprisingly, the Vreman model and the σ-model, which aim to avoid excessive artificial dissipation near walls, give larger WSS values particularly during accelerating flow. As the flow reaches its peak and decelerates towards the end of systole, only the two Smagorinsky model simulations exhibit significant backward stress, matching the higher OSI values seen in Table 8. Due to the
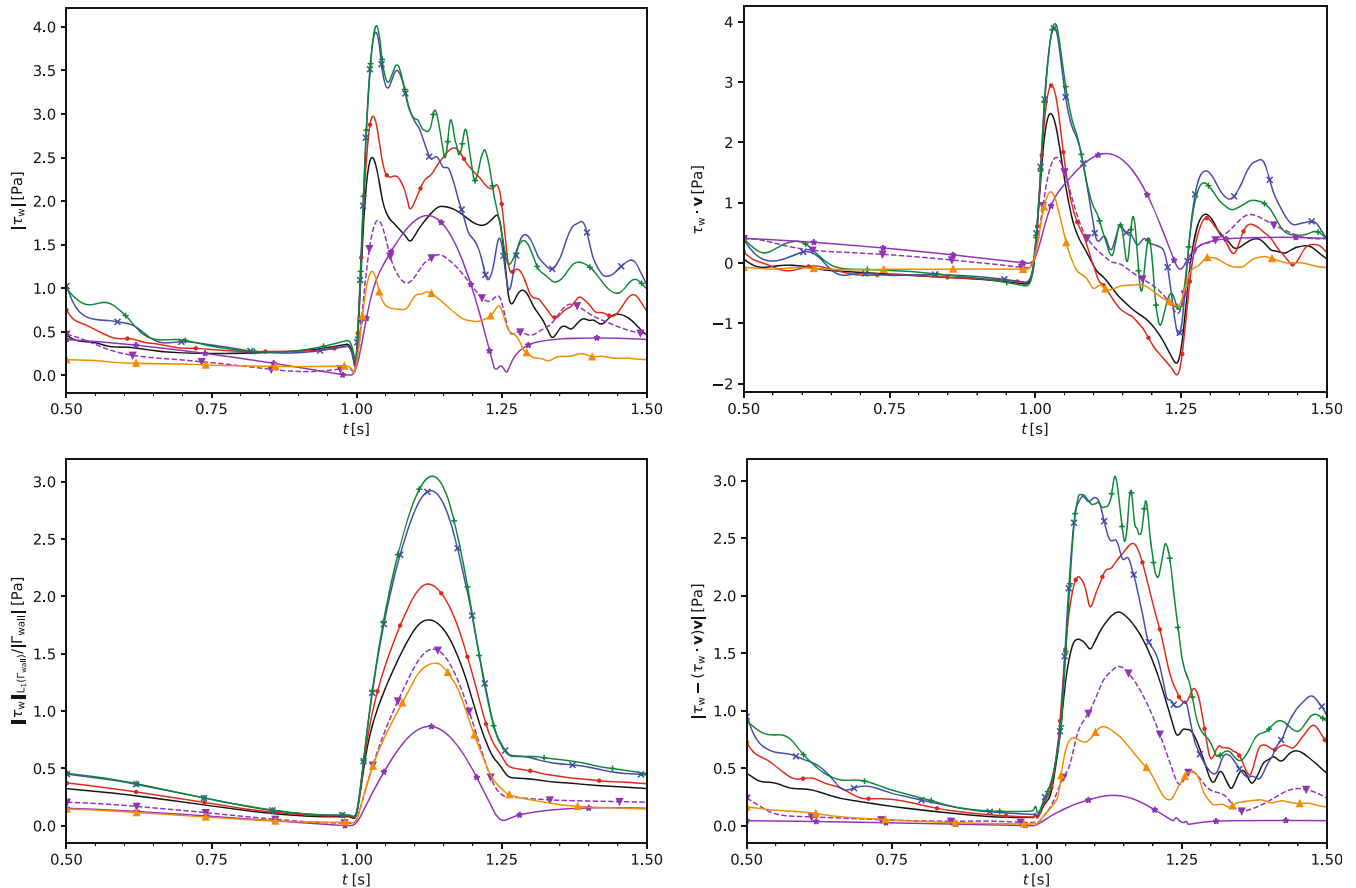

FIGURE 19 Upper left: spatially averaged wall shear stress magnitude over the reference patch. Upper right: spatially averaged forward wall shear stress over the reference patch. Lower left: spatially averaged wall shear stress magnitude over Γ_{wall}. Lower right: spatially averaged lateral wall shear stress over the reference patch. The legend is given in Figure 12.

TABLE 8 Time-averaged wall shear stress magnitude and OSI over reference patch.

Turbulence model	$|\tau_{\mathrm{w}}|$ (Pa)	OSI
Smagorinsky, $C_{\mathrm{Sma}} = 0.01$	0.77128	0.45779
Smagorinsky, $C_{\mathrm{Sma}} = 0.005$	0.96752	0.44082
Vreman, $C_{\mathrm{Vre}} = 0.07$	1.15169	0.29806
σ-model, $C_{\sigma} = 1.35$	1.22330	0.32456
RB-VMS, P_1/P_1 elements	0.50879	0.00662
RB-VMS, P_1/P_1 elements, fine mesh	0.52881	0.25779
RB-VMS, P_2/P_1 elements	0.32271	0.36761

smaller constant in the model, the curves for the Smagorinsky model with $C_{Sma} = 0.005$ in Figure 19 are usually closer to the Vreman and σ-model than the curves for $C_{Sma} = 0.01$. The latter results have some similarity with those computed with the RB-VMS model with second order velocity and the RB-VMS model with first order velocity on the fine grid.

Figure 20 demonstrates that, as with the cross-sectional quantities of interest, the wall shear stress on the reference patch does not change much from period to period, again with the exception of the σ-model. For the σ-model, the amplitude and timing of the oscillations associated with the vortices just above the reference patch during deceleration vary along with the vortices themselves.

Exemplarily, Figure 21 depicts the pointwise time-averaged WSS magnitude and OSI for the σ-model.
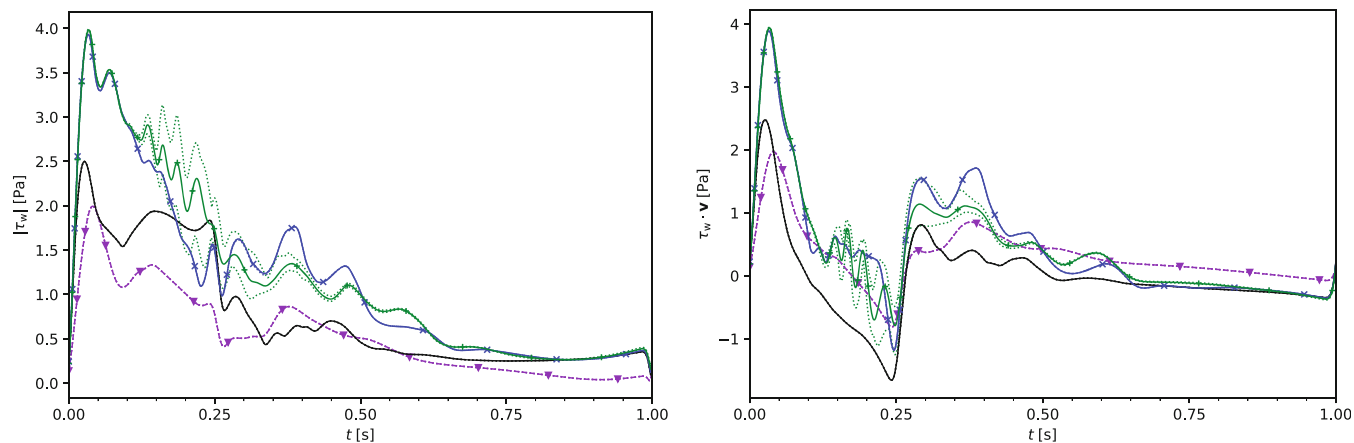

FIGURE 20 Left: spatially averaged wall shear stress magnitude over the reference patch during a heartbeat, averaging the results at the corresponding time instant over the simulated beats. Right: spatially averaged forward wall shear stress over the reference patch during a heartbeat, averaging the results at the corresponding time instant over the simulated beats. Dotted lines indicate period-wise minimum and maximum. The legend is given in Figure 12.
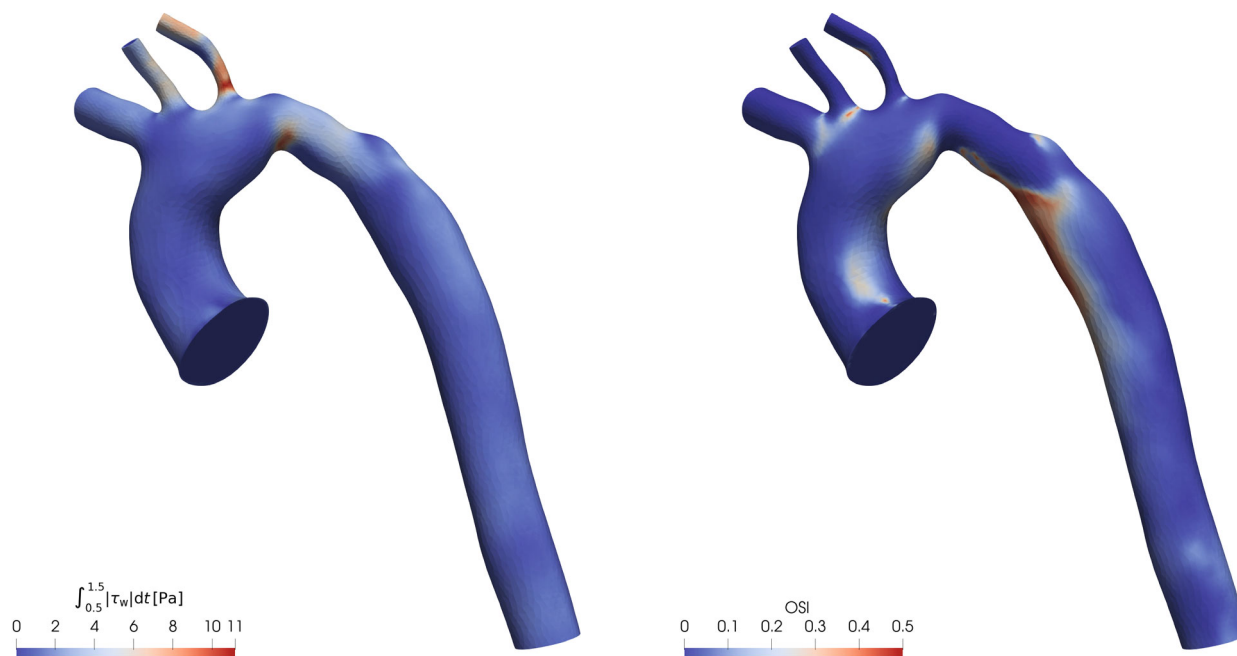

FIGURE 21 Left: time-averaged wall shear stress over the arterial wall for σ-model, $C_\sigma = 1.35$. Right: oscillatory shear index over the arterial wall for σ-model, $C_\sigma = 1.35$.

4.2.7 | Computational costs

The final comparison among the considered methods concerns the computational costs. The CPU times for each turbulence model are summarized in Table 9. Among the turbulence models with P_2/P_1 elements, there are only minor differences with respect to the computing time for both Smagorinsky models and the Vreman model. The σ-model was somewhat less efficient, which is likely due to the computation of the singular values. The RB-VMS model with P_2/P_1 elements needed considerably more time. There the reason is the lack of a good solver for the arising linear problems, as explained in Section 3.5. Finally, the most time-consuming simulations were those run on the fine grid, with the RB-VMS model and using P_1/P_1 elements.

Figure 22 breaks down the CPU time depending on the time step. This graph clearly shows the increased computational cost of computing the numerical solution in presence of rapid changes in the flow (during acceleration and deceleration at systole). Interestingly, the computational cost of using the RB-VMS model with P_2/P_1 elements on the coarse mesh increases above those of P_1/P_1 elements on the fine mesh, despite the smaller number of degrees of freedom.

5 | CONCLUSIONS AND OUTLOOK

This paper presented a study on the impact of the turbulence model that is used in numerical simulations of an aortic blood flow on clinically significant quantities of interest.

The computational model is based on a patient-specific mesh, and the numerical simulations have been tuned in order to match available inflow (velocity profile) and outflow (flow rates) measurements. Due to the lack of clinical data, the outflow boundary conditions have been restricted to purely resistive lumped parameter models (one parameter per outlet). This choice possesses an additional unknown parameter, the systemic vascular resistance. However, our

TABLE 9 CPU statistics for each model. Step time in units of seconds wall time per millisecond simulated time.

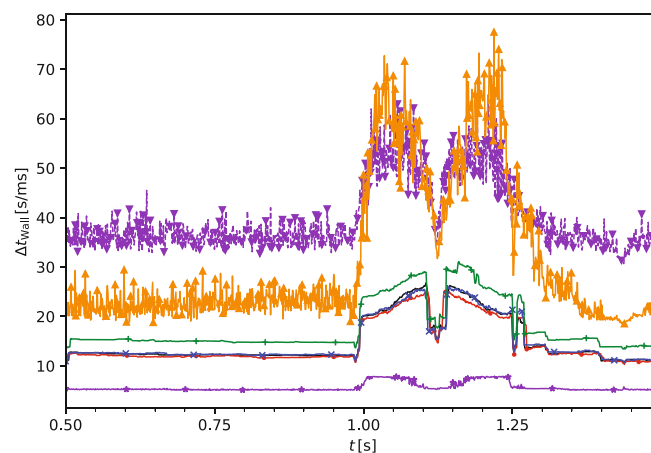| Turbulence model	Total wall time (h:min:s)	Average step time (s/ms)
Smagorinsky, $C_{\text{Sma}} = 0.01$	6:35:42.4	15.8
Smagorinsky, $C_{\text{Sma}} = 0.005$	6:25:23.9	15.4
Vreman, $C_{\text{Vre}} = 0.07$	6:34:45.0	15.8
σ-model, $C_\sigma = 1.35$	7:48:53.3	18.7
RB-VMS, P_1/P_1 elements	2:26:41.2	5.9
RB-VMS, P_1/P_1 elements, fine mesh	17:17:12.5	41.5
RB-VMS, P_2/P_1 elements	14:17:21.9	34.3

FIGURE 22 Computation time per output step. The legend is given in Figure 12.

numerical studies showed that the impact of this parameter on all quantities of interest is very small. As an alternative, more general models could be considered (e.g., 3-elements Windkessel models). These models might affect the time-dependent behavior of the quantities of interest, but it may be expected that the impact on averaged quantities would remain small. Furthermore, the fluid model assumed rigid vessel walls, neglecting fluid–structure interaction effects, which are out of the scope of the current work. Although this aspect could have a quantitative influence on the wall shear stresses, one can expect that it does not affect the qualitative differences between the turbulence models, which is the main focus of this study. The numerical simulations are based on the assumption of a Newtonian flow. Further studies taking into account non-Newtonian models have recently been published.[42]

The effect of the order of the finite element velocity space was investigated, exemplarily for the RB-VMS model. First-order velocity elements yielded results very different from the other models, while the agreement with other approaches considerably improved using second order velocity elements, suggesting, in our opinion, that the latter choice can achieve better accuracy. Using a piecewise linear velocity on a refined grid led often to a considerable increase of the agreement, but not always, as could be seen for the normalized flow displacement in Figure 17. Consequently, in our opinion, from the point of view of accuracy using second order velocity is the better choice.

Inspecting the results obtained with second order velocity simulations, one can divide the considered turbulence models into two groups. On the one hand, the Smagorinsky and the RB-VMS models and on the other hand, the Vreman and the σ-models. The results given by the models of each group were often, though not always, qualitatively similar. This division corresponds to the amount of numerical diffusion that is introduced by the models, particularly near walls and in transitional regions. Whereas the models from the first group computed rather smooth solutions, due to their comparatively large numerical diffusion, the flow fields predicted with the methods from the second group possess much more small eddies. In our opinion, the results with the less diffusive turbulence models are the more trustworthy ones. The σ-model was less dissipative in our simulations, but its computational costs were higher by a factor of around 1.2 compared to the Vreman model. The numerical results presented in this paper do not show a clear advantage in preferring one of these two models to the other.

In summary, this paper provides a quantification of the impact of different turbulence models on the prediction of relevant biomarkers for aortic blood flows. Based on the presented results, it can be concluded that the choice of the specific turbulence model is a very important step in the process of numerical modeling.

An interesting question not yet addressed by the studies presented here is the impact of local or uniform refinement in space and time on these differences, which are expected to disappear with spatial refinement as the mesh eventually becomes suitable for direct numerical simulation. A detailed study of this question using extended high-performance computations is the intended subject of future work.

ORCID
Sarah Katz https://orcid.org/0000-0001-6333-4962
Alfonso Caiazzo https://orcid.org/0000-0002-7125-8645

ENDNOTES

[a] See Section 4.1 for our choices.

[b] Stationary test functions, zero fine velocity on the boundary, velocity test function gradients orthogonal to fine velocity gradient.

[c] Here we used an iterative FGMRES/BiCGSTAB solver for the velocity problems (as for the whole system in the RB-VMS case) and a direct solver (MUMPS) for the pressure problems.

[d] FGMRES preconditioned with a few iterations of BiCGSTAB at each step, itself with a basic Jacobi preconditioner.

[e] Note that in the case of a perfectly circular cross-section, the hydraulic radius is half the geometric radius.

REFERENCES

1. De Mey S, Segers P, Coomans I, Verhaaren H, Verdonck P. Limitations of doppler echocardiography for the post-operative evaluation of aortic coarctation. *J Biomech*. 2001;34(7):951-960. doi:10.1016/S0021-9290(01)00043-4

2. Nielsen JC, Powell AJ, Gauvreau K, Marcus EN, Prakash A, Geva T. Magnetic resonance imaging predictors of coarctation severity. *Circulation*. 2005;111:622-628.

3. Stout KK, Daniels CJ, Aboulhosn JA, et al. 2018 AHA/ACC guideline for the Management of Adults with Congenital Heart Disease: a report of the American College of Cardiology/American Heart Association task force on clinical practice guidelines. *Circulation*. 2019; 139:e698-e800.

4. 2014 ESC guidelines on the diagnosis and treatment of aortic diseases: document covering acute and chronic aortic diseases of the thoracic and abdominal aorta of the adult. *Eur Heart J*. 2014;35(41):2873-2926. doi:10.1093/eurheartj/ehu281

5. Goubergrits L, Riesenkampff E, Yevtushenko P, et al. MRI-based computational fluid dynamics for diagnosis and treatment prediction: clinical validation study in patients with coarctation of aorta. *J Magn Reson Imaging*. 2015;41(4):909-916.

6. Schubert C, Brüning J, Goubergrits L, et al. Assessment of hemodynamic responses to exercise in aortic coarctation using MRI-ergometry in combination with computational fluid dynamics. *Sci Rep*. 2020;10:18894.

7. Goubergrits L, Mevert R, Yevtushenko P, et al. The impact of MRI-based inflow for the hemodynamic evaluation of aortic coarctation. *Ann Biomed Eng*. 2013;41:2575-2587.

8. Pietrasanta L, Zheng S, De Marinis D, Hasler D, Obrist D. Characterization of turbulent flow behind a transcatheter aortic valve in different implantation positions. *Front Cardiovasc Med*. 2022;8:804565.

9. Rigatelli G, Zuin M, Fong A, Tai TT, Nguyen T. Left main stenting induced flow disturbances on ascending aorta and aortic arch. *J Transl Int Med*. 2019;7(1):22-28.

10. Mittal R, Simmons SP, Udaykumar HS. Application of large-Eddy simulation to the study of pulsatile flow in a modeled arterial stenosis. *ASME J Biomech Eng*. 2001;123(4):325-332.

11. Perinajová R, Juffermans JF, Mercado JL, et al. Assessment of turbulent blood flow and wall shear stress in aortic coarctation using image-based simulations. *Biomed Eng Online*. 2021;20(1):84.

12. Andersson M, Karlsson M. Characterization of anisotropic turbulence behavior in pulsatile bloodflow. *Biomech Model Mechanobiol*. 2021;20:491-506.

13. Smagorinsky J. General circulation experiments with the primitive equations. *Mon Weather Rev*. 1963;91:99-164.

14. Vreman AW. An eddy-viscosity subgrid-scale model for turbulent shear flow: algebraic theory and applications. *Phys Fluids*. 2004;16(10): 3670-3681. doi:10.1063/1.1785131

15. Nicoud F, Toda HB, Cabrit O, Bose S, Lee J. Using singular values to build a subgrid-scale model for large eddy simulations. *Phys Fluids*. 2011;23(8):085106. doi:10.1063/1.3623274

16. Vergara C, Le Van D, Quadrio M, Formaggia L, Domanin M. Large eddy simulations of blood dynamics in abdominal aorticaneurysms. *Med Eng Phys*. 2017;47:38-46.

17. Xu H, Baroli D, Veneziani A. Global sensitivity analysis for patient-specific aortic simulations: the role of geometry, boundary condition and large Eddy simulation modeling parameters. *J Biomech Eng*. 2021;143:021012.

18. Bazilevs Y, Calo V, Cottrell J, Hughes T, Reali A, Scovazzi G. Variational multiscale residual-based turbulence modeling for large eddy simulation of incompressible flows. *Comput Methods Appl Mech Eng*. 2007;197(1):173-201. doi:10.1016/j.cma.2007.07.016

19. Ahmed N, John V. An assessment of two classes of variational multiscale methods for the simulation of incompressible turbulent flows. *Comput Methods Appl Mech Eng*. 2020;365:112997. doi:10.1016/j.cma.2020.112997

20. van der Palen RLF, Deurvorst Q, Kroft L, et al. Altered ascending aorta hemodynamics in patients after arterial switch operation for transposition of the great arteries. *Magn Reson Imaging*. 2020;51(4):1105-1116.

21. Feng Y, Wada S, Tsubota K, Yamaguchi T. A model-based numerical analysis in the early development of intracranial aneurysms. *Conf Proc IEEE Eng Med Biol Soc*. 2005;2006:607-610.

22. Si H. TetGen, a Delaunay-based quality tetrahedral mesh generator. *ACM Trans Math Softw*. 2015;41(2):1-36.

23. Bertoglio C, Caiazzo A, Bazilevs Y, et al. Benchmark problems for numerical treatment of backflow at open boundaries. *Int J Numer Methods Biomed Eng*. 2018;34(2):e2918.

24. Bruneau CH, Fabrie P. New efficient boundary conditions for incompressible Navier-stokes equations: a well-posedness result. *ESAIM: Math Model Numer Anal*. 1996;30(7):815-840. doi:10.1051/m2an/1996300708151

25. Braack M, Mucha PB. Directional do-nothing condition for the Navier-stokes equations. *J Comput Math*. 2014;32(5):507-521. doi:10.4208/jcm.1405-m4347

26. Bazilevs Y, Gohean J, Hughes T, Moser R, Zhang Y. Patient-specific isogeometric fluid-structure interaction analysis of thoracic aortic blood flow due to implantation of the Jarvik 2000 left ventricular assist device. *Comput Methods Appl Mech Eng*. 2009;198(45–46):3534-3550.

27. Esmaily Moghadam M, Bazilevs Y, Hsia TY, Vignon-Clementel IE, Marsden AL. A comparison of outlet boundary treatments for prevention of backflow divergence with relevance to blood flow simulations. *Comput Mech*. 2011;48:277-291.

28. Bertoglio C, Caiazzo A. A tangential regularization method for backflow stabilization in hemodynamics. *J Comput Phys*. 2014;261: 162-171.

29. Bertoglio C, Caiazzo A. A stokes-residual backflow stabilization method applied to physiological flows. *J Comput Phys*. 2016;313:260-278. doi:10.1016/j.jcp.2016.02.045

30. Dong S. A convective-like energy-stable open boundary condition for simulations of incompressible flows. *J Comput Phys*. 2015;302:300-328. doi:10.1016/j.jcp.2015.09.017

31. Ahmed N, Chacón Rebollo T, John V, Rubino S. A review of variational multiscale methods for the simulation of turbulent incompressible flows. *Arch Comput Methods Eng*. 2017;24(1):115-164. doi:10.1007/s11831-015-9161-0

32. Sagaut P, ed. *Large Eddy Simulation for Incompressible Flows*. third ed. Scientific ComputationSpringer-Verlag; 2006 An introduction, Translated from the 1998 French original, With forewords by Marcel Lesieur and Massimo Germano, With a foreword by Charles Meneveau.

33. John V. *Finite Element Methods for Incompressible Flow Problems*. Vol 51 of *Springer Series in Computational Mathematics*. Springer; 2016.

34. John V, Roland M. Simulations of the turbulent channel flow at $\mathrm{Re}_\tau = 180$ with projection-based finite element variational multiscale methods. *Int J Numer Methods Fluids*. 2007;55(5):407-429.

35. Lancellotti RM, Vergara C, Valdettaro L, Bose S, Quarteroni A. Large eddy simulations for blood dynamics in realistic stenotic carotids. *Int J Numer Methods Biomed Eng*. 2017;33(11):e2868. doi:10.1002/cnm.2868

36. Elman H, Howle VE, Shadid J, Shuttleworth R, Tuminaro R. Block preconditioners based on approximate commutators. *SIAM J Sci Comput*. 2006;27(5):1651-1668. doi:10.1137/040608817

37. Ahmed N, Bartsch C, John V, Wilbrandt U. An assessment of some solvers for saddle point problems emerging from the incompressible Navier-stokes equations. *Comput Methods Appl Mech Eng*. 2018;331:492-513. doi:10.1016/j.cma.2017.12.004

38. Elman H, Howle VE, Shadid J, Silvester D, Tuminaro R. Least squares preconditioners for stabilized Discretizations of the Navier-stokes equations. *SIAM J Sci Comput*. 2008;30(1):290-311. doi:10.1137/060655742

39. Wilbrandt U, Bartsch C, Ahmed N, et al. ParMooN—A modernized program package based on mapped finite elements. *Comput Math Appl*. 2017;74(1):74-88. doi:10.1016/j.camwa.2016.12.020

40. Ku D, Giddens D, Zarins C, Glagov S. Pulsatile flow and atherosclerosis in the human carotid bifurcation. Positive correlation between plaque location and low oscillating shear stress. *Arteriosclerosis*. 1985;5(3):293-302.

41. Klingensmith ME, Chen LE, Glasgow SC, Goers TA, Melby SJ. *The Washington Manual of Surgery*. fifth ed. Wolters Kluwer Health / Lippincott Williams & Wilkins; 2008.

42. Katz S, Caiazzo A, John V. Impact of viscosity modeling on the simulation of aortic blood flow. *J Comput Appl Math*. 2023;425:115036. doi:10.1016/j.cam.2022.115036